Geodynamic Setting and Cu-Ni Potential of Late Permian Xiwanggou Mafic-Ultramafic Rocks, East Kunlun Orogenic Belt, NW China

Jiandong Zhang[1,2], Miao Yu[1]*, Hui Wang[3], Bin Li[1], Chengyou Feng[2], J. M. Dick[1], Jinchao Li[4], Huilei Kong[4] and Zhiyi Zhao[5]

[1] Key Laboratory of Metallogenic Prediction of Nonferrous Metals and Geological Environment Monitor, Ministry of Education, Central South University, Changsha, China, [2] MNR Key Laboratory of Metallogeny and Mineral Assessment, Institute of Mineral Resources, Chinese Academy of Geological Science, Beijing, China, [3] Laboratory of Mineralization and Dynamics, Chang'an University, Xi'an, China, [4] MLR Key Laboratory for the Study of Focused Magmatism and Giant Ore Deposits, Xi'an Center of Geological Survey, China Geological Survey, Xi'an, China, [5] Qinghai Geological Survey Institute, Xining, China

Several magmatic Cu–Ni sulfide deposits have recently been explored along the deep Middle Kunlun fault related to the extension of the East Kunlun orogenic belt in Qinghai Province, NW China. The Xiwanggou mafic–ultramafic rocks associated with Cu–Ni sulfide mineralization are first to be dated as late Permian compared to most of the deposits formed during late Silurian–early Devonian in this region. The Xiwanggou complexes located in the junction area between the East Kunlun and West Qinling belts, are composed of gabbros, olivine-gabbros, pyroxenites, olivine-pyroxenites, and peridotites. The Cu–Ni mineralization are mainly hosted in the olivine-pyroxenites and pyroxenites, whereas the sulfide-poor mineralization distributed in gabbros and olivine-gabbros. Zircon LA-ICP-MS U–Pb dating of the gabbro and olivine-pyroxenite revealed their crystallized ages of 250.8 ± 0.8 Ma and 257.3 ± 0.7 Ma, respectively. The trace element characteristics of the Xiwanggou fertile mafic-ultramafic rocks shows the enrichments in Sr, Rb, Th, Ba and light rare earth elements, and depletions in Nb and Ta, which are associated with the slab derived fluid input and dehydration melting of amphiboles. Meanwhile, Sr–Nd and Hf isotopic compositions of the gabbro [εNd(t) = 0.66–1.18; εHf(t) = 5.2–12] and olivine-pyroxenite [εNd(t) = −1.09 − −0.43; εHf(t) = 5.4–17.7] show that the magma was mainly derived from the metasomatized portions of subcontinental lithospheric mantle (SCLM) source in the mantle wedge. The magma primarily experienced dehydration melting processes of amphiboles and subsequently underwent hydrated melting in the overlying mantle wedge and relatively reduced background. The cool subduction process of the Anemaqen oceanic lithosphere maybe trigger large melting in the mantle wedge resulting in a relative low-Ni content in the melt. The transpressional windows formed by the right-lateral strike-slip shearing action of the Wenquan and South Kunlun faults in the South Kunlun forearc belt created a significant conduit for the magma ascending. The thermometer of Fe and Ni exchange between coexisting olivine and sulfide melt indicates the magma were yielded in a temperature range of ca. 1200–1300°C and an oxygen fugacity

range of ca. –10.57 to –8.98 (log unit), which suggested that the parental magma of the Xiwanggou complex derived from a relatively reduced source favoring Ni relative to Fe in the melt. The intermediate sulfide segregation from the melt resulted in a medium tenor potential for the Xiwanggou complex.

Keywords: Xiwanggou, East Kunlun orogen, Cu-Ni sulfide deposit, late Permian, mafic–ultramafic rocks, zircon U–Pb dating, Sr–Nd isotope, Fe–Ni exchange

INTRODUCTION

Several magmatic Cu–Ni sulfide deposits have recently been explored along the deep Middle Kunlun fault paralleled to the extension of the East Kunlun orogenic belt (EKOB), Qinghai Province, NW China (Li et al., 2015; Song et al., 2016; Zhang Z. W. et al., 2016; Li et al., 2018). The Xiariham deposit with reserve of 1.16 Mt averaging grades of 0.65 wt% Ni, 0.14 wt% Cu, and 0.013 wt% Co, and the Shitoukengde deposit with 0.15 Mt averaging grades of 0.32% Ni were explored. And several new middle – small scale deposits, comprising Langmuri, Gayahe, Binggounan, and Xiwanggou mineralized locations have been discovered (**Figure 1A**; Zhang et al., 2015; He et al., 2017; Wang et al., 2020). The Xiwanggou mineralized mafic-ultramafic complex is located in the east of the EKOB, the northern part of the Qinghai-Tibet Plateau (**Figure 1**), which was first outlined by a team from the Xi'an Center, China Geological Survey during field mapping in 2015–2017. Several intrusions outcrop in the Xiwanggou area but only the olivine pyroxenites have been found to contain significant Ni–Cu sulfide mineralization.
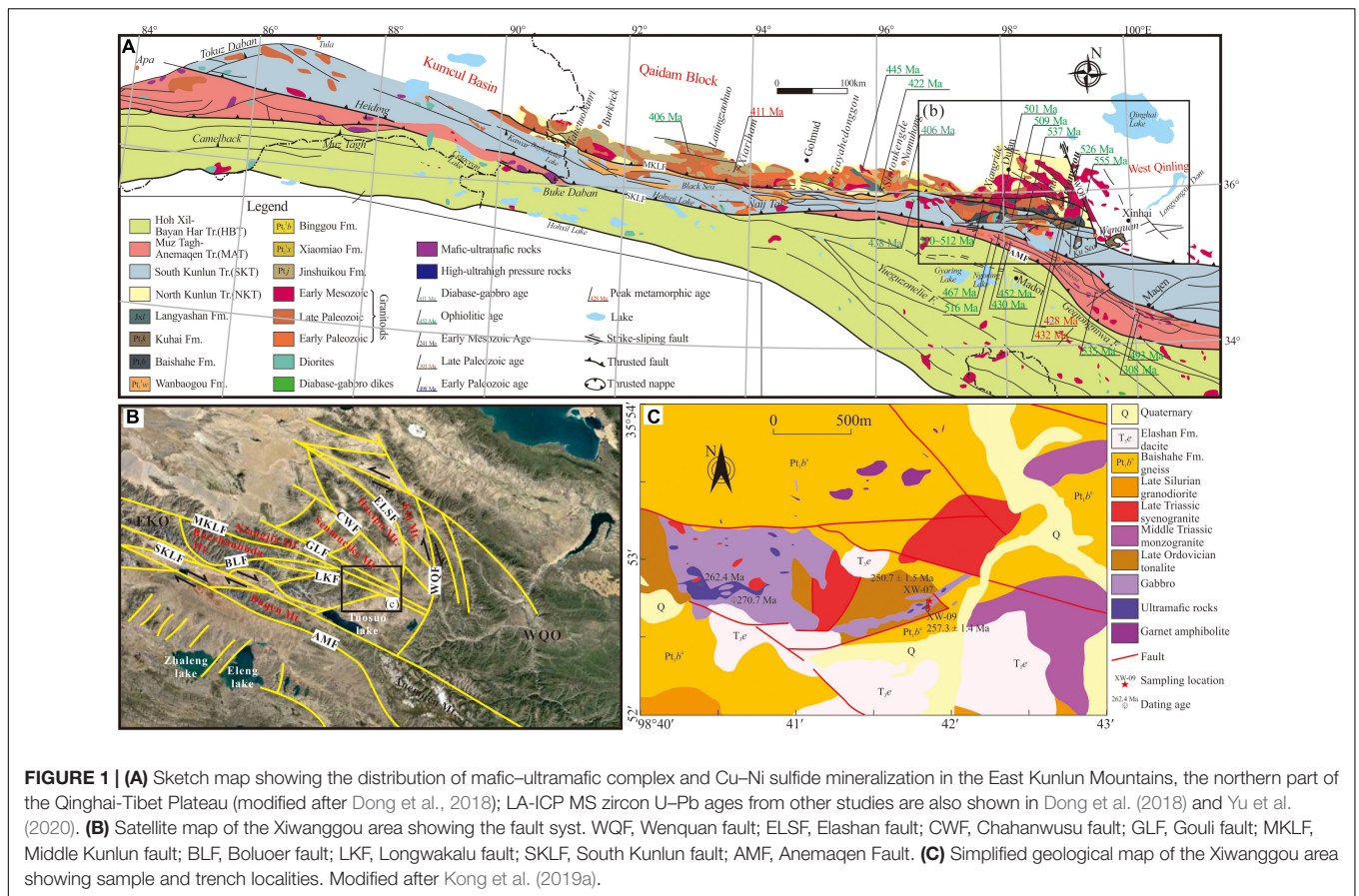
Most of the world's large magmatic sulfide deposits are interpreted to have formed in continental rift settings (Maier and Groves, 2011; Naldrett, 2013), where a mantle plume intersects a continental rift, and provides a large volume of magma with high metal content as a result of high degree partial melting (Barnes and Lightfoot, 2005). Moreover, most of the super-large magmatic sulfide deposits often occur in association with small differentiated intrusions, and an open system of protracted-flow magma conduits provides a significant space for ore reservoirs in a extensional environment (Song et al., 2010; Maier and Groves, 2011; Naldrett, 2013; Lightfoot and Evans-Lamswood, 2015; Barnes and Robertson, 2019). However, many magmatic Ni–Cu sulfide deposits have recently been discovered in orogenic settings or subduction-related magmatic arcs (Maier et al., 2008; Sappin et al., 2011), and they have significantly contributed Ni and Cu resources in China and the world. Examples of these include the Early Permian Kalatongke (33 Mt at 0.8 wt% Ni and 1.3 wt% Cu) (Song and Li, 2009; Li C. S. et al., 2012), and Huangshan-Jing'erquan Ni–Cu belt (>50 Mt at an average grade of 0.52 wt% Ni and 0.27 wt% Cu) in North Xinjiang (NW China), and the Early Carboniferous Ni–Cu ore deposits (16 Mt at 0.66 wt% Ni and 0.46% wt% Cu) hosted in the Aguablanca intrusion in Spain (Piña et al., 2006). Therefore, a few significant deposits are associated with the margins of large oceans or with supra-subduction zone environments, possibly reflecting poor preservation potential or, with the latter, limitations on plume interaction with continental lithosphere (Begg et al., 2010).

It is generally accepted that an extension or thinning environment including intracontinental rifting and post collisional extension are optimal for the formation of magmatic sulfide deposits in the EKOB magmatic Cu–Ni–Co mineralization under the Proto- and Paleo-Tethys evolution in the EKOB (Jiang et al., 2015; Zhang Z. W. et al., 2016; Zhang et al., 2021). The mafic-ultramafic complexes show diverse lithofacies with different formation ages, indicating the multiple stages of long-lived Paleozoic mantle-derived magmatism (Song et al., 2011; Wang et al., 2014; Peng et al., 2016), and most identify the ore-forming period as Late Silurian to Early Devonian, such as the Xiariham and Shitoukengde deposits (Wang et al., 2013; Sun et al., 2014; Song et al., 2016). However, the association of the Late Permian Xiwanggou mafic-ultramafic rocks with Cu–Ni sulfide mineralization has significantly broken the previous viewpoints and broadened the prospecting horizon.

The EKOB is generally considered to have been in an oceanic lithosphere subduction environment during late Permian (Zhang et al., 2012; Dong et al., 2018). At this point, we compares contrasting geochemical trends exhibited between fertile and barren late Permian basalts in the EKOB in terms of major and trace elements, Sr–Nd isotopic ratios and zircon Hf isotope to analyze the dynamic setting and ore-forming potential of the Xiwanggou complex. In addition, it is significant to know what the tectonic mechanism controls the conduit formation for the Xiwanggou complexes in a compressional subduction environment.

GEOLOGICAL SETTING

The EKOB is located in the western part of the central orogenic belt (**Figure 1A**), which trends east-west and is approximately 1,500 km long and 50–200 km wide. The EKOB is generally subdivided into four terranes from the north to the south: the North Kunlun, South Kunlun, Muztagh-Anemaqen and Hohxil-Bayanhar Terranes farthest south (**Figure 1A**; Yang et al., 1986; Jiang, 1992; Luo et al., 1999; Yu et al., 2020), which are bounded by the North Kunlun Fault (NKF), Middle Kunlun Fault (MKF), South Kunlun Fault (SKF), and Muztagh-Anemaqen Fault (MAF), respectively, from the north to the south (**Figure 1A**). The orogen is bounded by the Altun Fault to the west and Wenquan Fault to the east (**Figure 1A**). The NW-trending Wenquan fault is the boundary between the EKOB and the West Qinling orogenic belt (WQOB), and crosses the Elashan Mountains (**Figure 1A**). The Elashan Mountain is located in the easternmost segment of the EKOB, and in its eastern part,

FIGURE 1 | (A) Sketch map showing the distribution of mafic–ultramafic complex and Cu–Ni sulfide mineralization in the East Kunlun Mountains, the northern part of the Qinghai-Tibet Plateau (modified after Dong et al., 2018); LA-ICP MS zircon U–Pb ages from other studies are also shown in Dong et al. (2018) and Yu et al. (2020). **(B)** Satellite map of the Xiwanggou area showing the fault syst. WQF, Wenquan fault; ELSF, Elashan fault; CWF, Chahanwusu fault; GLF, Gouli fault; MKLF, Middle Kunlun fault; BLF, Boluoer fault; LKF, Longwakalu fault; SKLF, South Kunlun fault; AMF, Anemaqen Fault. **(C)** Simplified geological map of the Xiwanggou area showing sample and trench localities. Modified after Kong et al. (2019a).

the metamorphic basement and Pre-Mesozoic sedimentary rocks were uplifted due to the NE-dipping thrust fault systems and the Wenquan dextral strike-slip fault (Jiang et al., 2008). Previous studies suggested that the EKOB and WQOB were part of a unified orogen before the Wenquan fault system developed (Chen et al., 2015; Ren et al., 2016; Shao et al., 2017).

The tectonic evolution of the EKOB are closely associated with the assembling and colliding history of variable terranes in different era. The North Kunlun Terrane (NKT), as an active continental margin, hosted a large amount of Precambrian basement rock of Jinshuikou Group (Liu et al., 2005; He et al., 2016), and late Ordovician-middle Silurian calc-alkaline granitoids (Wu et al., 2012; Qi, 2015; Wang et al., 2016), which are related to the subduction of back arc oceanic lithosphere existed between the NKT and SKT at ca. 460 Ma causing the late Ordovician-middle Silurian magmatism in the NKT and thrusted basement rocks (Dong et al., 2018). The South Kunlun Terrane (SKT), which developed as an inner-oceanic island arc, consisted of the Wanbaogou Group basalts and large amounts of multistage felsic magmatic rocks (Cai and Wei, 2007; Zhang et al., 2010; Kong et al., 2014; Chen et al., 2016; Yu et al., 2020). Xu et al. (2016) got a zircon SIMS dating age of 762 ± 2 Ma for the Wanbaogou basalts, and their geochemical features are similar to those of oceanic island basalt. The Late Silurian to Early Devonian granitoids display either peraluminous or metaluminous features (Zhao et al., 2008; Shi et al., 2016), which

were possibly resulted from an transition from collisional to a post-collisional environment between the NKT and SKT during the Late Silurian-Middle Devonian (Long et al., 2006; Zhang D. X. et al., 2016). The Muztagh-Anemaqen Terrane (MAT) developed as a young island arc as a consequence of subduction of Proto-Tethys Oceanic crust, which carried SSZ (supra-subduction zone) type ophiolites (Wu et al., 2005; Li et al., 2017), together with island arc tholeiite (IAT) and TTGs (trondhjemite-tonalite-granodiorites) during the Early Paleozoic (Ren et al., 2012; Qi, 2015; Zhao et al., 2017). The collision between SKT and MAT probably occurred after the middle Devonian, as evidenced from the absence of the upper Devonian strata in the SKT (Ye et al., 2004). A new subduction zone reconstructed along the south of the MAT after the middle Permian, which resulted in extensive development of calc-alkaline granitoids in the NKT, SKT, and MAT (Zhang et al., 2006; Liu et al., 2015; Ma et al., 2015; Dong et al., 2016). The final closure of the Anemaqen Ocean might have occurred in the Late Triassic as indicated by dates from the upper Triassic Babaoshan terrestrial molasse formation (Wu et al., 2017).

The emplacement of mafic-ultramafic magma in the EKOB can be separated into two stages (Yu et al., 2020): (1) the first emplacement stage occurred primarily in the Late Silurian–Early Devonian (ca. 393–427 Ma); (2) the second stage occurred in the Middle-Late Permian. Previous studies indicate that the first stage complexes were probably emplaced

in a post-collisional extensional environment (Wang et al., 2014), and their components are mainly gabbro, pyroxenite, and peridotite facies rocks (Peng et al., 2016). In addition, the first stage intrusions generally developed extensive Cu–Ni sulfide mineralization that are mainly hosted in the pyroxenite and peridotite outcrop in the Xiariham, Binggounan, Shitoukengde, Akchucsai, and Langmuri areas (Sun et al., 2014; Li et al., 2015; Song et al., 2016; He et al., 2017; Zhang et al., 2018). In the second stage, the mafic-ultramafic complexes outcrop mainly in the Jiadang, Bairiqili, and Xiwanggou areas (Xiong et al., 2011a; Kong et al., 2018). In the first two areas, gabbro is the dominant rock type, and no sulfide ore bodies have been found, but the Xiwanggou mafic–ultramafic complex is first discovered containing Cu–Ni sulfide mineralization including chalcopyrite, pyrrhotite, and pentlandite, which predominantly are hosted in the olivine gabbros and olivine pyroxenites.

PETROGRAPHY AND MINERALIZATION

The Xiwanggou mafic–ultramafic complex is mainly composed of gabbro, olivine gabbro, and olivine pyroxenite facies rocks, in which younger mafic gabbroic intrusions emplacing into the older ultramafic bodies (**Figures 1C, 2A**), both of which show strong differentiation. The complexes underwent extensive alteration by serpentinization and amphibolization. The richest ore bodies are hosted in the ultramafic rocks (**Figures 2D–G**), while some lower grade ones are found in the mafic rocks (**Figures 2B,C**). The olivine gabbro contains a few disseminated sulfides (**Figure 2C**), and is mainly composed of 20–30% olivine, 30–40% clinopyroxene, and 20–30% labradorite, in addition to a few hornblende and secondary chlorite minerals (**Figures 3a,b**). The gabbro has an equigranular texture that is characterized by euhedral pyroxenes and plagioclases (**Figure 2C**), and is predominately composed of 20–30% clinopyroxene, 50–60% plagioclase, and <10% hornblende with accessory apatite and zircon (**Figures 3c,d**). Olivine pyroxenite contains 40–50% olivine and 40% clinopyroxenes, plus hornblende, biotite and sulfide. Pyroxenes commonly occur as large oikocrysts enclosing olivine crystals to form a poikilitic texture (**Figures 3b,d**). The sulfide assemblages including pentlandite, pyrrhotite, and chalcopyrite occur in the interstitial spaces of olivine or pyroxene cumulates (**Figures 2D–G, 3g,h**). A gabbro vein intruded into the olivine pyroxenite (**Figure 2A**), suggesting that the gabbro formed slightly later than the olivine pyroxenite.

The intrusions were prominently controlled by the NEE and EW fault systems, and extend 1.2 km along the NEE direction with a 100–200 m width. The country rocks hosting the complex are Baishahe Formation and are dominated by Precambrian metamorphic rocks such as biotite schist, quartz-rich schist, quartzite, marble, and gneiss. Small late Ordovician tonalite stocks were cut by the Xiwanggou mafic–ultramafic intrusive rocks in the area (**Figure 1C**). No ages for the granodiorite stocks are currently available, but papers in preparation will give zircon U–Pb ages for the quartz diorite and granodiorite stocks.

The Xiwanggou mafic-ultramafic rocks have undergone variable degrees of post emplacement hydrothermal alteration. Olivine is partially altered to serpentine; clinopyroxene is partially replaced by amphibole and calcite (**Figures 3c,e,f**); plagioclase is partially replaced by chlorite (**Figure 3a**); and secondary magnetite (**Figure 3h**) occurs in the micro-fractures of base-metal sulfides and envelopes the sulfides. In the areas not affected by faulting and deformation, alteration is weak (30% collectively) but pervasive. In the areas affected by faulting and deformation, alteration is far more intensive, up to 100% in places.

SAMPLING AND ANALYTICAL METHOD

All the samples used in this study were collected in the exploratory trench in the central part of the Xiwanggou mafic–ultramafic complexes where the best sulfide mineralization develops (**Figure 1C**). Different types of sulfide mineralization and host rocks were systematically sampled along the trench. Highly altered and deformed outcrops were avoided. Zircon crystals separated from the sulfide-poor gabbro samples (XW-07) and sulfide-rich samples olivine pyroxenite (XW-09) were used for zircon U–Pb dating. Six hand samples are made into polished thin sections to observe the mineral components and be termed. In addition, two samples are made into powder to analyze the chemical and isotopic components.

Zircon LA–ICP–MS U–Pb Dating

Zircon selection and targeting, and transmission and reflected light and cathode luminescence imaging works were conducted at Beijing Zhongxing Meike Technology Co. Ltd. Zircon crystals with various aspect ratios and colors were separated from the samples and inlayed into an epoxy resin target and then polished, cleaned and carbon coated. The cathode luminescence (CL) and back-scatted electron images were photographed to identify zoning patterns in zircons. Some of good patterns were chose for further dating and Hf isotope analysis. The CL images were conducted using a FEI Quanta450 electron microscope, and back-scatted electron images were made with a Gatan MonoCL4, with a voltage of 15 kV.

The U–Pb dating and rare element analyses of zircons was conducted synchronously using laser ablation inductively coupled plasma mass spectrometry (LA-ICP-MS) at the Yanduzhongshi Geological Analysis Laboratories Ltd. Laser Ablation System used was a New Wave UP213, and ICP-MS was a Brooke M90. During the laser ablation process, helium gas was the carrier gas and argon gas was used as the compensation gas to adjust sensitivity, and the two gases were mixed through a homogenizer before entering the ICP-MS. The analysis of each sample point included a blank signal of about 20∼30 s and a sample signal of 50 s. Both a 91500 zircon standard and Plešovice were used as external standards for isotope fractionation correction (Wiedenbeck et al., 1995; Sláma et al., 2008). The actual diameter of LA denudation spots was 25 μm. Concordia diagrams and weighted mean calculations were made using
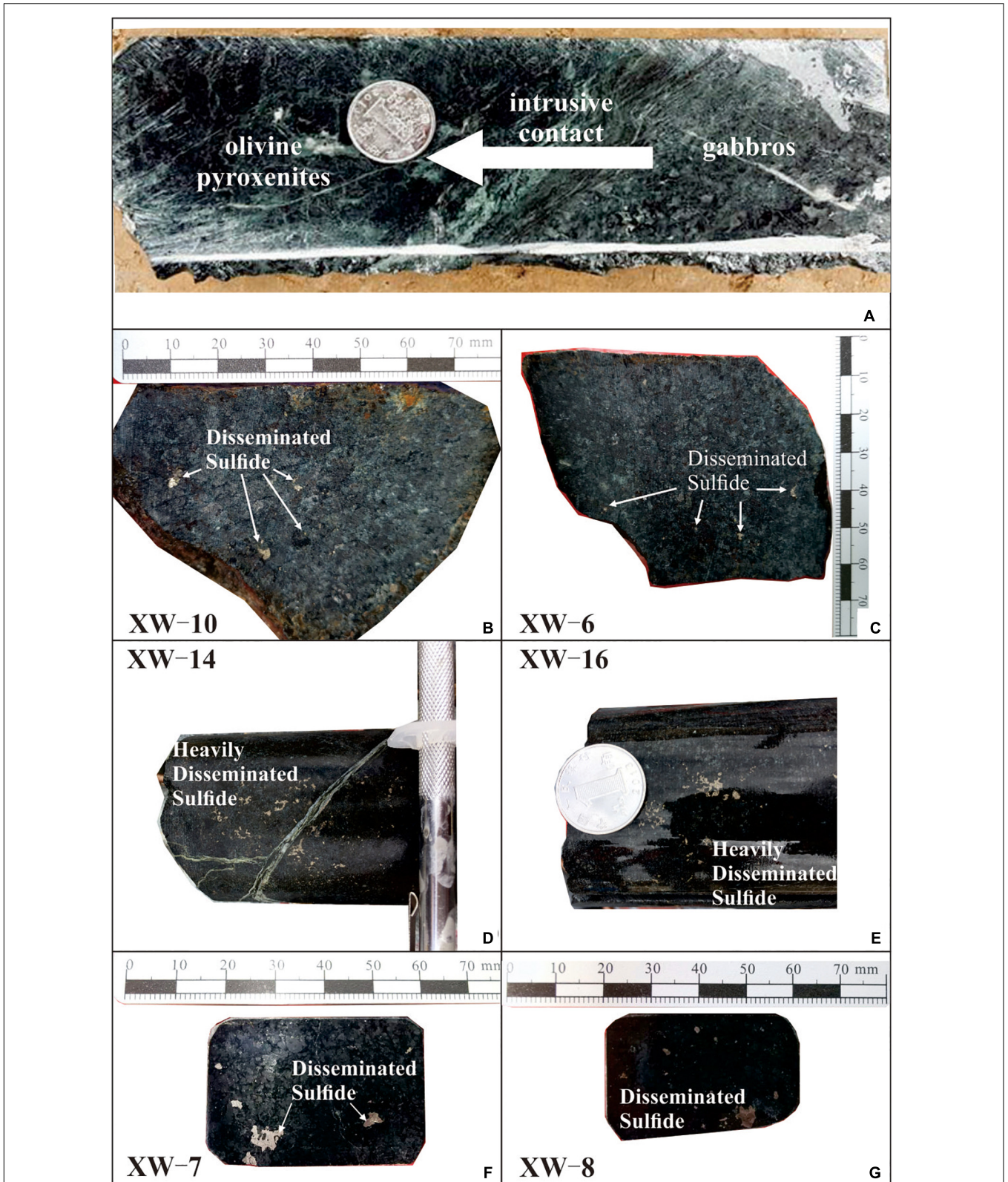
FIGURE 2 | Hand specimen photos of the Xiwanggou mafic-ultramafic rocks. **(A)** The intrusive contact relationship between olivine pyroxenite and gabbro; **(B,C)** Disseminated Cu–Ni sulfide minerals developed in gabbro and olivine gabbro, respectively; **(D–G)** Disseminated Cu–Ni sulfide minerals in olivine pyroxenite.
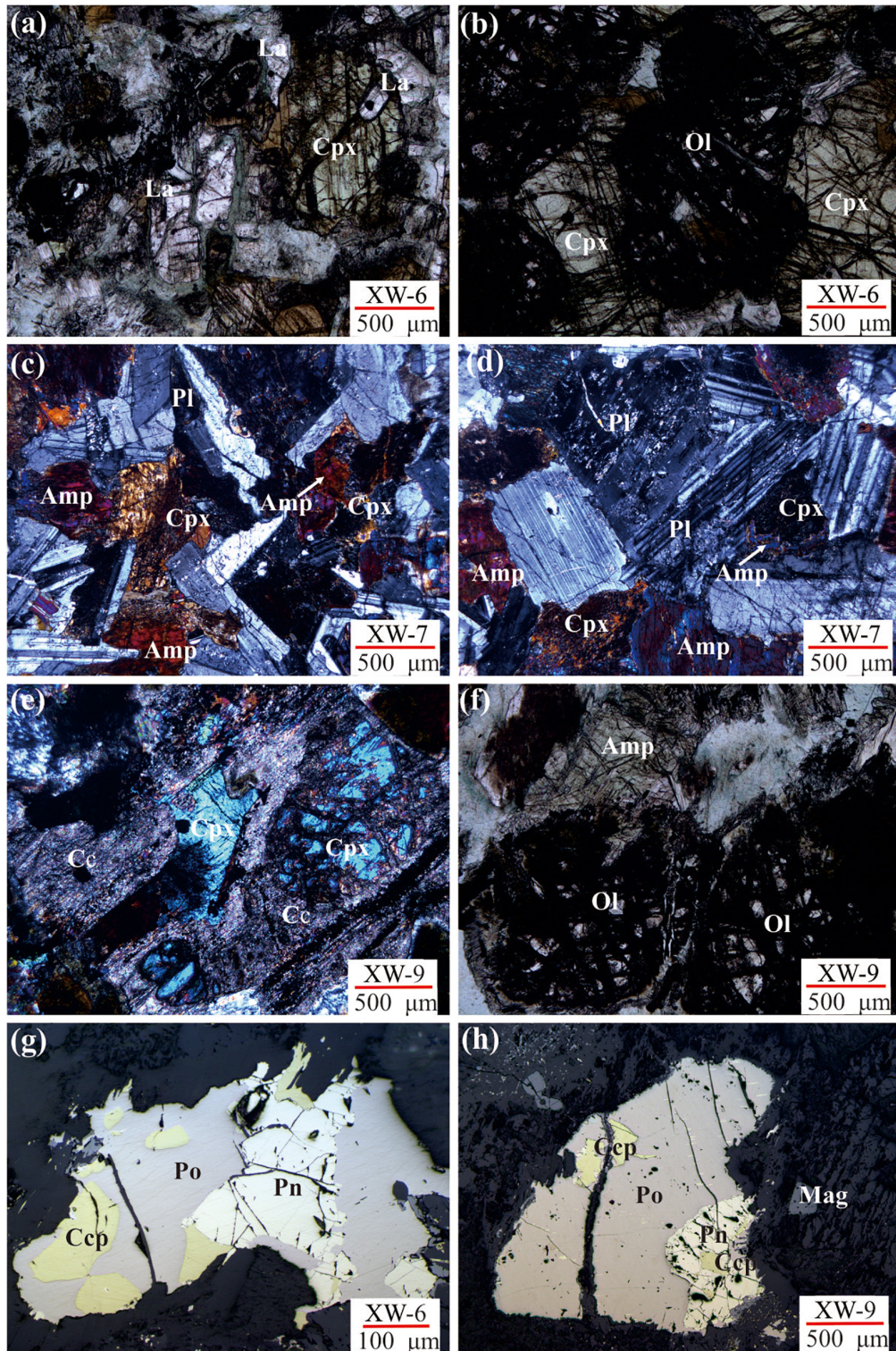
FIGURE 3 | Microphotographs of the Xiwanggou intrusions (**a,b,f**: plain polarized, **c–e**: cross polarized, **g,h**: reflected light). **(a)** some euhedral labradorite clinopyroxene developed in an olivine gabbro sample; **(b)** Medium-grained and severely absorbed olivine surrounded by clinopyroxene in an olivine gabbro sample; **(c,d)** Euhedral clinopyroxene and plagioclase showing equigranular texture filled by fine-grained and interstitial amphibole in a gabbro sample. **(e)** Severe carbonation altered clinopyroxene in a gabbro sample; **(f)** Medium-grained and severely absorbed olivine surrounded by amphibole in an olivine pyroxenite sample; **(g,h)** the pentlandite, pyrrhotite, and chalcopyrite in mineralized olivine gabbros and olivine pyroxenites, respectively; Amp, amphibole; Cpx, clinopyroxene; La, labradorite; Ol, olivine; Pl, plagioclase; Pn, pentlandite; Po, pyrrhotite; Ccp, chalcopyrite; Mag, magnetite.

FIGURE 4 | Cathodoluminescence images of selected zircon crystals from the Xiwanggou **(A)** and gabbro **(B)**. Circles are laser beam targets. The black numbers are $^{206}Pb/^{238}U$ ages (Ma), and the red numbers are εHf(t) values.
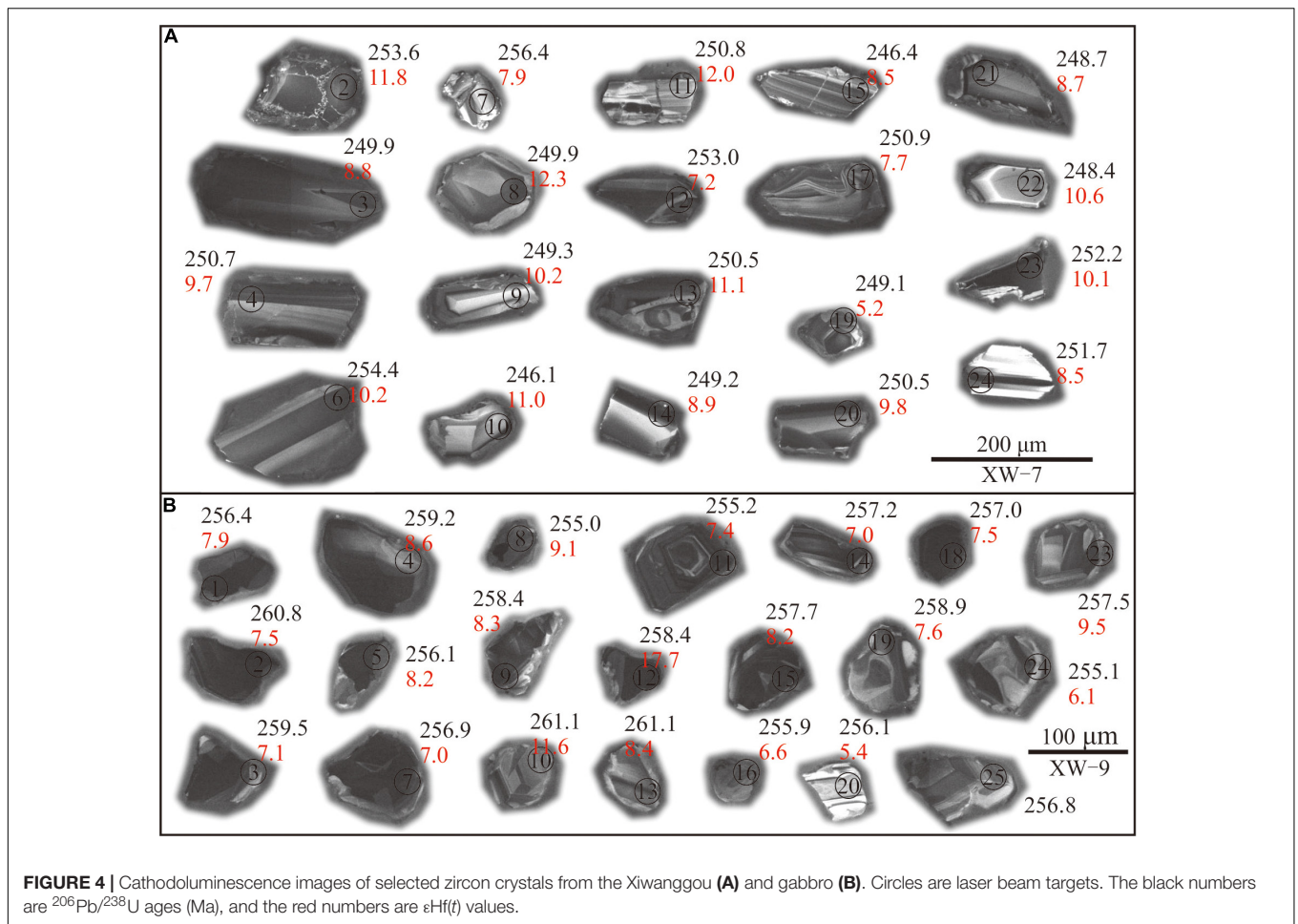
ZSKits authorized by the Yanduzhongshi Geological Analysis Laboratories Ltd.

In situ Hf Isotopic Analyses

In situ zircon Hf isotopic analyses were performed using a Geolas Pro laser ablation system coupled to a Neptune multi-collector ICP-MS at the Key Laboratory for the Study of Focused Magmatism and Giant Ore Deposits, MLR, at the Xi'an Center of Geological Survey, China Geological Survey. The detailed instrumental conditions and data acquisition procedures are similar to those described by Hou et al. (2007). A stationary laser ablation spot with a beam diameter of 30 μm was used for the analyses. The ablated aerosol was carried by helium and combined with argon in a mixing chamber before being introduced to the ICP-MS plasma. All of the Hf analyses were performed on the same spots that underwent U–Pb laser ablation analysis. The GJ-1 zircon standard was used as a reference standard; during this study, it yielded a weighted mean $^{176}Hf/^{177}Hf$ ratio of 0.282030 ± 40 (2SE).

Electron Microprobe Analysis

In this study, olivine, pyroxene and sulfide hosted in the mafic-ultramafic rocks were analyzed. EPMA X-ray elemental analysis were conducted through a 4 WDS detector-equipped Shimadzu EMPA-1720H (Tokyo, Japan) electron microprobe at Key Laboratory of Metallogenic Prediction of Nonferrous Metals and Geological Environment Monitoring (Central South University), Ministry of Education. Operating conditions were 15 kV acceleration, 20 nA beam current, and 5 μm diameter electron beam. Silicon, Ti, Al, Fe, Mn, Mg, Ca, Na, K, Cr, Co, and Ni were analyzed. The back-scatter electronic (BSE) images were photographed under 15 Kv accelerating voltage and 0.5 nA current beam.

Whole-Rock Major and Trace Elements

The major and trace element analysis for the bulk rock samples was mainly performed in the Yanduzhongshi Geological Analysis Laboratories Ltd. Fresh samples were first broken to centimeter sizes; only the fresh pieces were selected, washed with deionized water, dried and then ground to less than 200 mesh (0.5200 ± 0.0001 g) for geochemical analyses. Sample powders were fluxed with Li2B4O7 (1:8) to make homogeneous glass disks at 1250°C using a V8C automatic fusion machine produced by the Analymate Company in China. The bulk rock major elements were analyzed using X-ray fluorescence spectrometry techniques (Zetium, PANalytical). The analytical errors for major elements
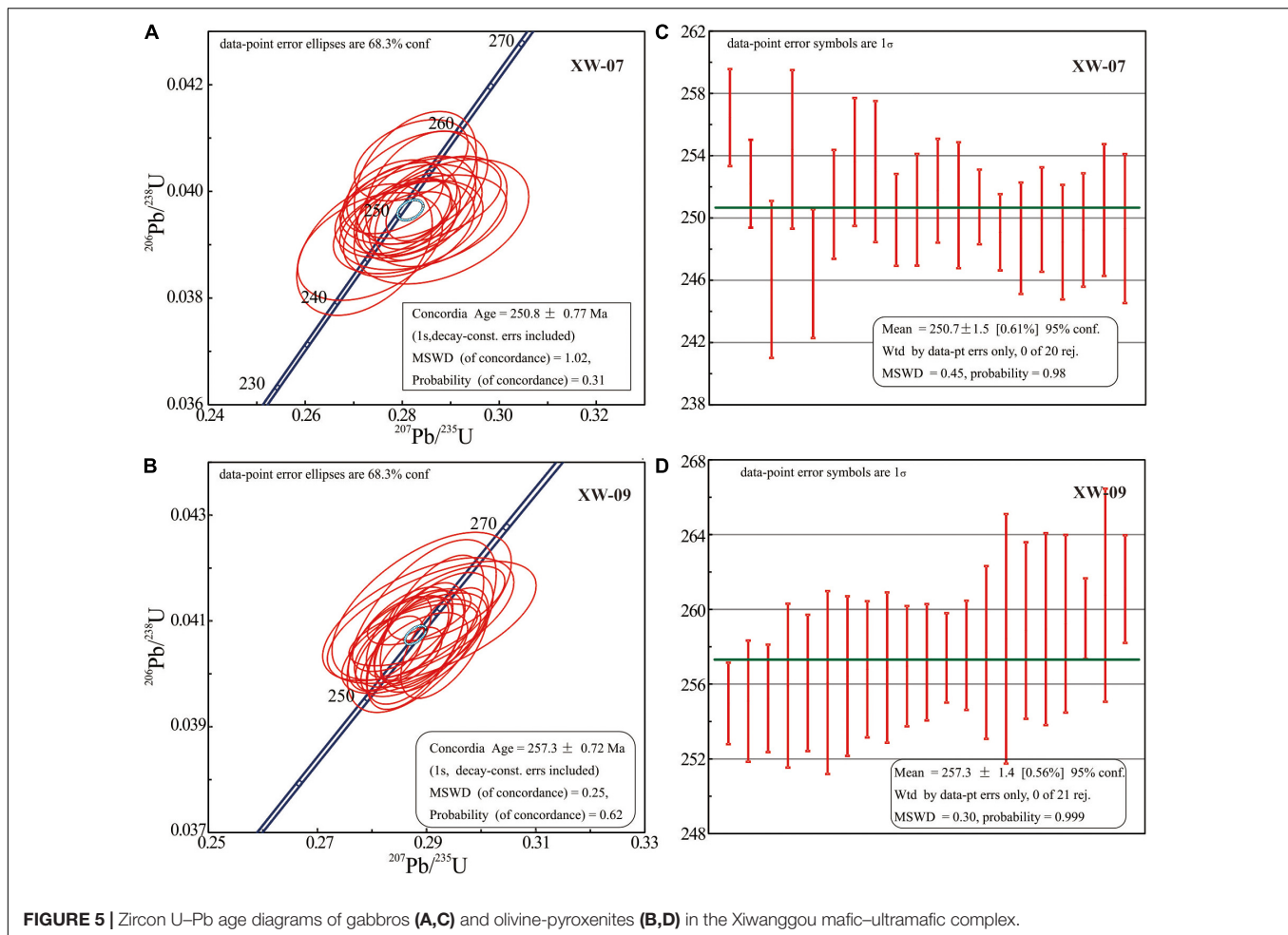
TABLE 1 | Concentrations of ^{238}U and ^{232}Th, and U–Pb isotopes of zircon from the Xiwanggou mafic–ultramafic complex.

Sample	U^{238} (μ g/g)	Th^{232} (μ g/g)	U/Th	Pb^{207}/Pb^{206}	1 σ	Pb^{207}/U^{235}	1 σ	Pb^{206}/U^{238}	1 σ	Pb^{206}/U^{238} (Ma)	1 σ
XW-07-02	256	250	1.02	0.05106	0.00164	0.28309	0.00959	0.04012	0.00066	253.6	4.1
XW-07-03	264	120	2.20	0.05165	0.00130	0.28016	0.00666	0.03952	0.00048	249.9	3.0
XW-07-04	663	573	1.16	0.05174	0.00082	0.28329	0.00437	0.03966	0.00039	250.7	2.4
XW-07-06	574	464	1.24	0.05072	0.00122	0.28271	0.00830	0.04025	0.00082	254.4	5.1
XW-07-07	225	95	2.38	0.05041	0.00143	0.28187	0.00772	0.04058	0.00050	256.4	3.1
XW-07-08	488	551	0.88	0.05218	0.00118	0.28319	0.00580	0.03953	0.00054	249.9	3.4
XW-07-09	124	139	0.89	0.05319	0.00203	0.28809	0.01189	0.03943	0.00077	249.3	4.8
XW-07-10	279	228	1.22	0.05063	0.00134	0.27222	0.00922	0.03891	0.00081	246.1	5.0
XW-07-11	156	132	1.18	0.05216	0.00165	0.28288	0.00812	0.03968	0.00065	250.8	4.0
XW-07-12	1231	1054	1.17	0.05128	0.00095	0.28395	0.00759	0.04002	0.00073	253.0	4.5
XW-07-13	517	700	0.74	0.05245	0.00145	0.28737	0.00939	0.03962	0.00068	250.5	4.2
XW-07-14	149	172	0.86	0.05248	0.00212	0.28432	0.01136	0.03942	0.00059	249.2	3.6
XW-07-15	247	350	0.71	0.05100	0.00178	0.27337	0.00986	0.03897	0.00067	246.4	4.1
XW-07-17	306	80	3.81	0.05138	0.00164	0.27926	0.00794	0.03968	0.00056	250.9	3.5
XW-07-19	427	287	1.49	0.05180	0.00108	0.28157	0.00640	0.03939	0.00039	249.1	2.4
XW-07-20	154	163	0.94	0.05163	0.00176	0.28131	0.01001	0.03963	0.00058	250.5	3.6
XW-07-21	475	271	1.75	0.05164	0.00179	0.28123	0.01018	0.03933	0.00058	248.7	3.6
XW-07-22	153	148	1.03	0.05249	0.00162	0.28139	0.00891	0.03929	0.00059	248.4	3.7
XW-07-23	302	193	1.56	0.05060	0.00121	0.27810	0.00684	0.03990	0.00046	252.2	2.8
XW-07-24	188	343	0.55	0.05194	0.00203	0.28378	0.01095	0.03983	0.00054	251.7	3.3
XW-09-01	2893	1674	1.78	0.05259	0.00096	0.29331	0.00530	0.04058	0.00069	256.4	4.3
XW-09-02	1612	0	0.00	0.05093	0.00141	0.28910	0.01086	0.04128	0.00092	260.8	5.7
XW-09-03	1227	884	1.42	0.05084	0.00120	0.28865	0.00627	0.04108	0.00035	259.5	2.2
XW-09-04	401	736	0.55	0.05104	0.00174	0.28848	0.01157	0.04103	0.00077	259.2	4.8
XW-09-05	1557	1483	1.05	0.05187	0.00106	0.28807	0.00592	0.04052	0.00079	256.1	4.9
XW-09-07	2649	1653	1.44	0.05105	0.00086	0.28523	0.00633	0.04065	0.00065	256.9	4.0
XW-09-08	5029	1293	1.76	0.05161	0.00082	0.28721	0.00372	0.04034	0.00035	255.0	2.2
XW-09-09	1616	1631	1.00	0.05150	0.00175	0.28910	0.00902	0.04090	0.00108	258.4	6.7
XW-09-10	560	365	1.58	0.05159	0.00129	0.29361	0.00709	0.04133	0.00047	261.1	2.9
XW-09-11	1739	351	5.23	0.05092	0.00081	0.28324	0.00413	0.04039	0.00046	255.2	2.9
XW-09-12	2101	1394	1.52	0.05165	0.00102	0.29100	0.00626	0.04099	0.00083	258.9	5.1
XW-09-13	488	268	1.92	0.05123	0.00141	0.28755	0.00777	0.04074	0.00039	257.4	2.4
XW-09-14	1890	337	5.69	0.05082	0.00062	0.28490	0.00393	0.04070	0.00050	257.2	3.1
XW-09-15	1445	266	5.55	0.05180	0.00090	0.29131	0.00717	0.04078	0.00075	257.7	4.6
XW-09-16	1260	615	1.48	0.05173	0.00108	0.28790	0.00590	0.04050	0.00071	255.9	4.4
XW-09-18	3083	1423	2.20	0.05116	0.00061	0.28721	0.00453	0.04067	0.00052	257.0	3.2
XW-09-19	262	169	1.56	0.05153	0.00206	0.29095	0.01264	0.04097	0.00076	258.9	4.7
XW-09-20	350	45	9.44	0.05162	0.00161	0.28719	0.00840	0.04052	0.00059	256.1	3.6
XW-09-23	669	816	0.83	0.05075	0.00095	0.28554	0.00603	0.04076	0.00047	257.5	2.9
XW-09-24	846	577	1.72	0.05161	0.00108	0.28775	0.00646	0.04036	0.00052	255.1	3.2
XW-09-25	363	518	0.69	0.05173	0.00148	0.28894	0.00803	0.04064	0.00059	256.8	3.6

were better than 1%. For trace element analysis, sample powders were first dissolved using distilled HF + HNO3 in a screw-top Teflon beaker for 4 days at 100°C. Trace elements of those samples were analyzed by inductively coupled mass spectrometry (ICP-MS) at the Yanduzhongshi Geological Analysis Laboratories Ltd. The analytical uncertainty of the elements examined was better than 5% for ICP-MS analysis, except for a few samples with low trace element content, for which the uncertainty was about 10%. The obtained trace element values in the GSR-2 standard were all consistent with their recommended values.

Sr–Nd Isotope Analysis

Main analysis process is as follows: a 0.25 g sample was placed in a Teflon stewing pot; 0.5 ml HNO_3 and 1.5 ml of HF were added, and the container was closed; the sample underwent heating digestion for 48 h at 190°C; HF was expelled at 160°C, and 3 ml 1:1 HNO_3 was added at 150°C; the container was closed and the temperature was maintained at 150°C for 6 h, and leaving constant mass to 25 g. Extraction of Sr was performed by spinning the appropriate solution in a centrifuge, and drying the

FIGURE 5 | Zircon U–Pb age diagrams of gabbros **(A,C)** and olivine-pyroxenites **(B,D)** in the Xiwanggou mafic–ultramafic complex.

supernatant; the acidity was adjusted; Sr was separated and purified using SR special resin. Extraction of Nd was similar to the extraction of Sr, but LN specific resin was used to separate and purify Nd. The $^{87}Sr/^{86}Sr$ ratios were measured on a Thermo Fisher Scientific multi-receiver ICP-MS and the and $^{143}Nd/^{144}Nd$ ratios were measured on a Neptune Plus Mc-ICP-MS in the Yanduzhongshi Geological Analysis Laboratories Ltd. The measured $^{88}Sr/^{86}Sr$ and $^{143}Nd/^{144}Nd$ ratios were normalized for mass fractionation using $^{88}Sr/^{86}Sr$ = 8.373209 and $^{143}Nd/^{144}Nd$ = 0.7218 respectively.

ANALYTICAL RESULTS

Zircon U–Pb Isotope Age

Cathode luminescence images of the selected zircon crystals from the Xiwanggou sulfide bearing gabbro and olivine-pyroxenite are shown in **Figure 4**. They are mostly wide stubby and columnar with a clear stripped texture at the edge. The long axis of the zircons from XW-07 (gabbro) are variable, from 50 to 250 μm, and those from XW-09

(olivine pyroxenite) range between 50 and 150 μm. The length-width ratios are between 1:1 and 2:1. Most of zircons show oscillatory zoning and inherited cores, but internally a few zircons are texturally homogeneous. These features indicate the selected zircons are of a magmatic origin from the mafic-ultramafic complexes.

The analytical results of the U–Pb isotopic dating are listed in **Table 1**. The zircon grains have 45–1653 μg/g Th, 124–5029 μg/g U, and U/Th ratios of 0.63–9.44. The U/Th ratio of magmatic zircons is generally less than 10; whereas the U/Th of metamorphic zircons is greater than 10 (Rubatto and Gebauer, 2000). This is consistent with our interpretation that all the grains are from magmatic zircons. The concordia plots of the analyses are shown in **Figures 5A,B**, and the average age plots are shown in the **Figures 5C,D**. The concordia plot shows a zircon U–Pb isotope age for the Xiwanggou sulfide-poor garbbo of 250.8 ± 0.77 Ma (**Figure 5A**), and its weighted age is 250.7 ± 1.5 Ma (**Figure 5C**). The concordia plot shows a zircon U–Pb isotope age for the sulfide-rich olivine-pyroxenite of 257.3 ± 0.72 Ma (**Figure 5B**), and its weighted age is 257.3 ± 1.4 Ma (**Figure 5D**). The results show that there is a large age gap of ∼ 7 Ma between the mafic and ultramafic associated with mineralization.

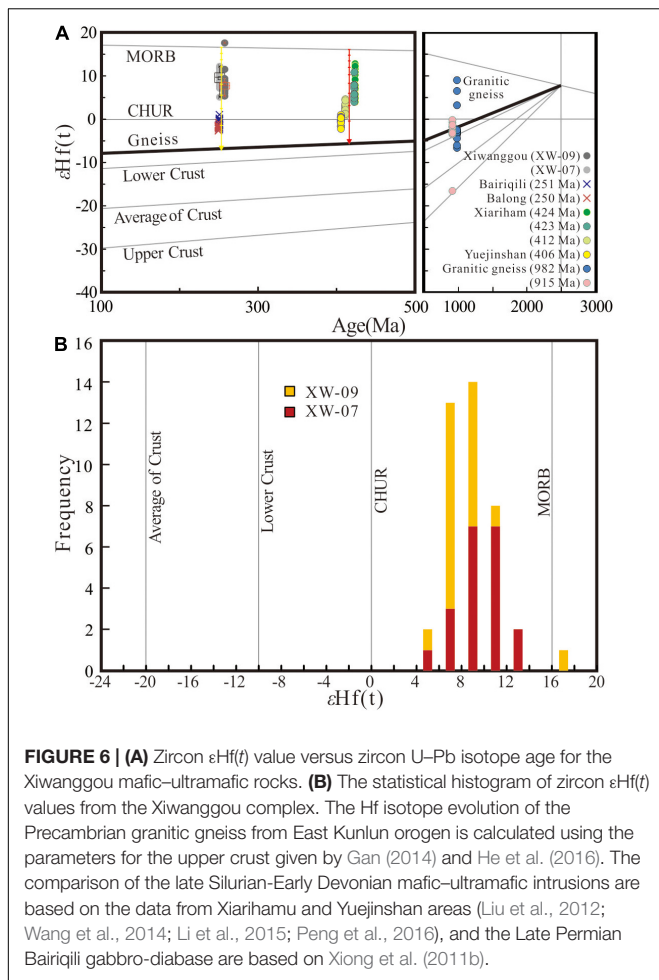**TABLE 2 |** MC-ICP-MS zircon Lu–Hf isotopic compositions from the Xiwanggou mafic–ultramafic complex.

Sample	age	$^{176}Yb/^{177}Hf(corr)$	2σ	$^{176}Lu/^{177}Hf(corr)$	2σ	$^{176}Hf/^{177}Hf(corr)$	2σ	eHf (T)	TDM	TDMC	fs
XW-07-02	250.8	0.065209	0.000353	0.001776	0.000011	0.282958	0.000023	11.8	426	525	−0.95
XW-07-03	250.8	0.018209	0.000423	0.000529	0.000011	0.282866	0.000027	8.8	540	719	−0.98
XW-07-04	250.8	0.074527	0.000435	0.002079	0.000010	0.282901	0.000031	9.7	512	656	−0.94
XW-07-06	250.8	0.069588	0.000391	0.001956	0.000017	0.282915	0.000026	10.2	490	624	−0.94
XW-07-07	250.8	0.024615	0.000438	0.000690	0.000014	0.282843	0.000021	7.9	576	774	−0.98
XW-07-08	250.8	0.054090	0.000389	0.001607	0.000009	0.282971	0.000030	12.3	404	492	−0.95
XW-07-09	250.8	0.040387	0.000520	0.001128	0.000011	0.282908	0.000023	10.2	489	630	−0.97
XW-07-10	250.8	0.033413	0.000658	0.000961	0.000015	0.282931	0.000024	11.0	455	577	−0.97
XW-07-11	250.8	0.024161	0.000428	0.000709	0.000008	0.282960	0.000022	12.0	411	509	−0.98
XW-07-12	250.8	0.055200	0.001563	0.001590	0.000041	0.282828	0.000023	7.2	610	816	−0.95
XW-07-13	250.8	0.015963	0.000137	0.000450	0.000002	0.282933	0.000023	11.1	445	566	−0.99
XW-07-14	250.8	0.100246	0.003047	0.002631	0.000088	0.282881	0.000028	8.9	549	707	−0.92
XW-07-15	250.8	0.088039	0.000546	0.002463	0.000014	0.282867	0.000024	8.5	567	737	−0.93
XW-07-17	250.8	0.036838	0.001071	0.001005	0.000028	0.282837	0.000028	7.7	588	789	−0.97
XW-07-19	250.8	0.073293	0.000361	0.002041	0.000009	0.282773	0.000028	5.2	698	946	−0.94
XW-07-20	250.8	0.025506	0.000324	0.000734	0.000010	0.282897	0.000026	9.8	500	652	−0.98
XW-07-21	250.8	0.044156	0.000413	0.001221	0.000012	0.282868	0.000023	8.7	547	721	−0.96
XW-07-22	250.8	0.056651	0.000331	0.001431	0.000009	0.282922	0.000023	10.6	474	603	−0.96
XW-07-23	250.8	0.050193	0.002320	0.001435	0.000065	0.282909	0.000023	10.1	492	631	−0.96
XW-07-24	250.8	0.034403	0.000689	0.000904	0.000012	0.282862	0.000027	8.5	552	733	−0.97
XW-09-01	257.3	0.023660	0.000205	0.000609	0.000006	0.282838	0.000024	7.9	580	779	−0.98
XW-09-02	257.3	0.015845	0.000051	0.000502	0.000002	0.282826	0.000035	7.5	595	805	−0.98
XW-09-03	257.3	0.022233	0.000143	0.000563	0.000003	0.282816	0.000026	7.1	611	830	−0.98
XW-09-04	257.3	0.002906	0.000060	0.000076	0.000002	0.282857	0.000028	8.6	547	731	−1.00
XW-09-05	257.3	0.006253	0.000057	0.000174	0.000001	0.282844	0.000030	8.2	565	760	−0.99
XW-09-07	257.3	0.011385	0.000064	0.000259	0.000002	0.282810	0.000019	7.0	614	839	−0.99
XW-09-08	257.3	0.013233	0.000105	0.000401	0.000004	0.282870	0.000025	9.1	533	705	−0.99
XW-09-09	257.3	0.002606	0.000063	0.000062	0.000001	0.282846	0.000019	8.3	561	755	−1.00
XW-09-10	257.3	0.005199	0.000034	0.000154	0.000002	0.282941	0.000024	11.6	431	542	−1.00
XW-09-11	257.3	0.028089	0.000257	0.000812	0.000008	0.282825	0.000026	7.4	602	810	−0.98
XW-09-12	257.3	0.076114	0.000234	0.002547	0.000007	0.283125	0.000057	17.7	186	149	−0.92
XW-09-13	257.3	0.020316	0.000632	0.000393	0.000012	0.282852	0.000024	8.4	559	747	−0.99
XW-09-14	257.3	0.012864	0.000306	0.000327	0.000012	0.282810	0.000025	7.0	615	839	−0.99
XW-09-15	257.3	0.004513	0.000042	0.000114	0.000001	0.282843	0.000026	8.2	566	762	−1.00
XW-09-16	257.3	0.007368	0.000306	0.000256	0.000010	0.282800	0.000025	6.6	629	863	−0.99
XW-09-18	257.3	0.017092	0.000551	0.000373	0.000010	0.282825	0.000023	7.5	596	807	−0.99
XW-09-19	257.3	0.002477	0.000051	0.000069	0.000002	0.282828	0.000029	7.6	586	796	−1.00
XW-09-20	257.3	0.002330	0.000067	0.000081	0.000003	0.282766	0.000028	5.4	672	937	−1.00
XW-09-23	257.3	0.008891	0.000027	0.000213	0.000002	0.282881	0.000023	9.5	515	679	−0.99
XW-09-24	257.3	0.008955	0.000119	0.000245	0.000003	0.282786	0.000027	6.1	648	894	−0.99

Hf Isotope

The Lu–Hf isotopes of the selected zircon crystals from the Xiwanggou mafic-ultramafic rocks are listed in **Table 2**. The calculated εHf(*t*) values of these zircon crystals are all positive varying from 5.2 to 12 for gabbro and 5.4 to 17.7 for olivine pyroxenite, respectively. A comparison of these values with those for depleted mantle, a potential contaminant, and the Precambrian granitic gneiss which is exposed in the Xiariham and Bokalike areas in the western part of the EKOB (data from Gan, 2014; He et al., 2016) is shown in **Figure 6**.

Mineral Compositions

The compositions of important rock-forming minerals such as olivine and pyroxenes are listed in **Tables 3, 4**. Olivine occurs as a cumulate phase in olivine gabbro, and commonly encloses chromite with olive crystals and exhibits a reactional rim in contacts with other silicate crystals. Minor amounts of olivine grains are encapsulated by pyroxene with olivine texture and serpentinization. The interiors of subhedral and euhedral olivine grains are often intersected by some serpentine veins. The composition of major elements has little change in the

FIGURE 6 | (A) Zircon εHf(*t*) value versus zircon U–Pb isotope age for the Xiwanggou mafic–ultramafic rocks. **(B)** The statistical histogram of zircon εHf(*t*) values from the Xiwanggou complex. The Hf isotope evolution of the Precambrian granitic gneiss from East Kunlun orogen is calculated using the parameters for the upper crust given by Gan (2014) and He et al. (2016). The comparison of the late Silurian-Early Devonian mafic–ultramafic intrusions are based on the data from Xiarihamu and Yuejinshan areas (Liu et al., 2012; Wang et al., 2014; Li et al., 2015; Peng et al., 2016), and the Late Permian Bairiqili gabbro-diabase are based on Xiong et al. (2011b).

samples (**Table 3**) with MgO = 44.34–45.13 wt.%, FeO = 14.61–15.43 wt.%, SiO$_2$ = 39.36–40.42 wt.%, NiO = 0.12–0.25 wt.%, Cr$_2$O$_3$ = 0–0.06 wt.% and a corresponding Fo value of 83.45–84.51 with an average of 84.08, which corresponds to chrysolite (**Figures 7A–F**). The good negative linear relationship between MgO (wt.%) and FeO (wt.%) in olivine indicates that there was a substitution between MgO (wt.%) and FeO (wt.%) (**Figure 7A**). Olivine contains 83.45–84.51 mol% Fo with an average of 84.08 mol% (which is the value for chrysolite), and it is depleted in Mn and Ca.

Pyroxene is mostly euhedral and subhedral grains, from a cumulate phase with olivine or olivine inclusions forming olivine texture. Serpentinization, chloritization, talcification, and fibrillation are common. Pyroxene consists mainly of clinopyroxene with SiO$_2$ content of 52.38–52.45 wt.%, TiO$_2$ content of 0.18–0.7 wt.%, Al$_2$O$_3$ content of 2.87–3.13 wt.%, FeO content of 4.13–4.26 wt.%, MgO content of 16.85–17wt.%, CaO content of 22.97–23.01 wt.%, Cr$_2$O$_3$ content of 1.13–1.34, and NiO content of 0–0.05 (**Figures 7A–F**).

Whole Rock Major and Trace Elements

The concentrations of major and trace elements in the samples from the Xiwanggou mafic–ultramafic intrusions are given as

Supplementary Table 1. In this study, the Xiwanggou samples can be geochemically divided into two groups based on the variability of SiO$_2$ and (K$_2$O + Na$_2$O) contents: 46.62–49.51 wt.% SiO$_2$ and 2.46–3.0 wt.% (K$_2$O + Na$_2$O) for gabbro; and 41.35–42.49 wt.% SiO$_2$ and 1.06–1.61 wt.% (K$_2$O + Na$_2$O) for olivine pyroxenites. The corresponding Mg$^{\#}$ of two groups are 77.76–82.04 and 88.10–88.22, respectively (**Figure 8**). The TiO$_2$ contents of all samples are very low, ranging from 0.16 wt.% to 0.74 wt.% (ave. 0.38 wt.%), which is significantly lower than that of oceanic tholeiite (2.63 wt.%), intraplate basalt (2.23 wt.%), but more similar to that of island arc basalt (0.98 wt.%). In summary, the gabbro in the Xiwanggou area is characterized by low Si and Ti, high Mg, and depleted alkali.

Primitive mantle-normalized diagrams for incompatible elements also exhibit nearly identical element concentrations, reflecting a similar abundance and composition for mafic–ultramafic rocks (**Figure 9A**). The abundances of more incompatible large ion lithophile elements (LILE) are greater than those of the high field strength elements (HFSE). This is typical of the mantel magmas proposed to possess a large lithospheric crust component. Other notable features include the depletion of Nb and Ta relative to La and U, enrichment of Sr relative to Pr and Nd, and slight depletion of Ba relative to Rb and Th. Such trace element patterns are clearly similar to those of island arc sulfide-bearing mafic intrusive rocks in the Tati and Selebi-Phikwe belts, eastern Botswana (Maier et al., 2008).

Almost all samples are uniformly enriched in LREE relative to HREE with (La/Sm)$_N$ of 1.43–2.38, and show flat HREE chondrite-normalized patterns with (Gd/Yb)$_N$ = 1.31–1.52 (**Figure 9B**). The gabbro has relatively higher total REE content (ΣREE = 20.46–42.76 ppm) and lower (La/Yb)$_N$ ratios [(La/Yb)$_N$ = 2.82–3.17] than that of olivine pyroxenite [ΣREE = 15.45–24.92 ppm; (La/Yb)$_N$ = 3.63–4.8]. Most of the samples have slightly negative Eu anomalies (Eu/Eu* = 0.80–0.95).

Sr–Nd Isotopes

The Rb–Sr and Sm–Nd isotope data for the Xiwanggou mafic-ultramafic rocks are given in **Table 5**. The initial isotopic ratios for the olivine pyroxenite and gabbro were calculated using the zircon U–Pb ages of 257.3 and 250.8 Ma for these two different intrusive phases, respectively. The olivine pyroxenite and gabbro samples have distinctive ^{147}Sm/^{144}Nd ratio range of 0.15406–0.158684 and 0.170205–0.17175, respectively. The olivine pyroxenites have slightly lower initial ^{143}Nd/^{144}Nd ratios varying narrowly between 0.512251 and 0.51285 than that of gabbros varying from 0.512629 to 0.512655. The (^{87}Sr/^{86}Sr)$_i$ ratios of the olivine pyroxenite range from 0.705535 to 0.706133, and the gabbro has a ratio (^{87}Sr/^{86}Sr)$_i$ of 0.705905–0.706620 (**Figure 10A**). In addition, the (^{87}Sr/^{86}Sr)$_i$ values of the Xiwanggou complex almost keep invariable with varying SiO$_2$ contents (**Figure 10A**). However, the (^{87}Sr/^{86}Sr)$_i$ values of the late Permian Bairiqili non-mineralization gabbro increase with raising SiO$_2$ contents (**Figure 10A**). The εNd(*t*) values of the olivine pyroxenite and gabbro are from −1.09 to −0.43 and 0.66 to 1.18, respectively (**Figure 10B**).

TABLE 3 | The composition of microprobe analysis of olivine in olivine gabbro from the Xiwanggou deposit.

Sample (wt.%)	X20111	x105.1	x10121	x10101	x109.1	X6011.1	X609.1	X608.3	X603.1	X602.1	X601.3	X902.1	Oli03	Oli	Oli	Oli
SiO_2	40.34	39.82	39.65	39.53	38.84	39.70	39.92	40.40	39.77	40.51	40.37	40.34	40.92	40.66	40.48	40.67
TiO_2	0.02	0.02	0.00	0.00	0.02	0.00	0.00	0.04	0.01	0.05	0.00	0.03	0.00	0.01	0.03	0.03
Al_2O_3	0.01	0.04	0.02	0.01	0.02	0.03	0.02	0.03	0.03	0.01	0.02	0.01	0.01	0.03	0.00	0.00
FeO	15.36	12.92	14.32	15.14	15.26	14.81	14.85	14.59	14.91	14.78	15.08	14.75	14.58	15.25	15.09	15.14
MnO	0.24	0.24	0.23	0.21	0.23	0.25	0.22	0.21	0.23	0.20	0.23	0.21	0.23	0.25	0.24	0.23
MgO	45.22	46.41	45.23	45.15	44.35	45.41	45.12	44.89	44.87	45.31	44.87	45.37	44.13	44.08	44.64	44.40
CaO	0.03	0.05	0.04	0.05	0.04	0.05	0.06	0.06	0.05	0.04	0.06	0.08	0.06	0.05	0.07	0.13
Na_2O	0.01	0.02	0.00	0.01	0.00	0.00	0.02	0.00	0.00	0.00	0.00	0.01	0.00	0.01	0.00	
K_2O	0.01	0.00	0.01	0.01	0.00	0.00	0.02	0.00	0.00	0.00	0.00	0.00	0.00	0.01	0.00	
Cr_2O_3	0.00	0.00	0.00	0.00	0.00	0.02	0.00	0.00	0.00	0.02	0.00	0.00	0.01	0.06	0.00	0.00
NiO	0.12	0.16	0.20	0.23	0.22	0.22	0.21	0.22	0.20	0.24	0.25	0.13	0.18	0.14	0.17	0.15
Total	101.25	99.51	99.50	100.11	98.77	100.25	100.22	100.22	99.87	100.89	100.62	100.81	99.93	100.35	100.54	100.60
Mg × 100/(Mg + Fe)	74.64	78.22	75.96	74.89	74.40	75.41	75.23	75.47	75.05	75.41	74.85	75.47	75.17	74.30	74.73	74.58
Si	1.000	0.995	0.997	0.992	0.989	0.993	0.998	1.007	0.998	1.004	1.005	1.002	1.022	1.015	1.008	1.013
Ti	0.000	0.000	0.000	0.000	0.000	0.000	0.000	0.001	0.000	0.001	0.000	0.001	0.000	0.000	0.001	0.001
Al	0.000	0.001	0.001	0.000	0.001	0.001	0.000	0.001	0.001	0.000	0.001	0.000	0.000	0.001	0.000	0.000
Fe	0.318	0.269	0.300	0.317	0.324	0.309	0.310	0.304	0.312	0.306	0.313	0.306	0.304	0.317	0.314	0.314
Mn	0.005	0.005	0.005	0.005	0.005	0.005	0.005	0.004	0.005	0.004	0.005	0.004	0.005	0.005	0.005	0.005
Mg	1.671	1.729	1.695	1.688	1.684	1.693	1.682	1.669	1.679	1.674	1.665	1.680	1.642	1.640	1.658	1.648
Ca	0.001	0.001	0.001	0.001	0.001	0.001	0.001	0.002	0.001	0.001	0.001	0.002	0.002	0.001	0.002	0.003
Na	0.000	0.001	0.000	0.001	0.000	0.000	0.001	0.000	0.000	0.000	0.000	0.001	0.000	0.000	0.000	0.000
K	0.000	0.000	0.000	0.000	0.000	0.000	0.001	0.000	0.000	0.000	0.000	0.000	0.000	0.000	0.000	0.000
Cr	0.000	0.000	0.000	0.000	0.000	0.000	0.000	0.000	0.000	0.000	0.000	0.000	0.000	0.001	0.000	0.000
Ni	0.002	0.003	0.004	0.005	0.005	0.004	0.004	0.004	0.004	0.005	0.005	0.003	0.004	0.003	0.003	0.003
Mole percent (mol%)																
Forsterite	83.81	86.30	84.74	84.01	83.64	84.34	84.24	84.42	84.11	84.39	83.97	84.42	84.18	83.55	83.88	83.77
Tephroite	0.25	0.25	0.24	0.23	0.25	0.26	0.23	0.23	0.24	0.21	0.24	0.22	0.25	0.27	0.25	0.24
Fayalite	15.94	13.45	15.01	15.77	16.11	15.40	15.52	15.36	15.65	15.40	15.79	15.36	15.57	16.17	15.87	15.98

TABLE 4 | The composition of microprobe analysis of pyroxene in olivine gabbro from the Xiwanggou deposit.

Sample (wt.%)	X6-11.2	X6-9.2	X6-8.2	X6-8.1	X6-7.2	X6-7.1	X6-3.2	X6-1.3	X6-1.2	X6-1.2	X6-1.1
SiO_2	51.33	50.99	50.77	50.82	52.19	51.83	51.53	51.38	51.37	51.90	51.27
TiO_2	0.50	0.41	0.52	0.51	0.53	0.45	0.49	0.55	0.54	0.53	0.51
Al_2O_3	3.65	3.12	3.05	3.37	3.07	3.23	2.83	3.52	3.05	3.01	3.41
FeO	4.06	4.06	4.34	3.91	4.06	4.08	4.70	4.04	4.60	4.23	3.96
MnO	0.11	0.14	0.11	0.10	0.13	0.11	0.13	0.11	0.14	0.14	0.11
MgO	17.00	17.21	17.24	17.74	16.89	16.89	17.07	16.93	17.62	17.41	16.72
CaO	21.35	21.49	21.28	20.54	21.98	21.39	21.02	21.30	20.29	21.07	21.80
Na_2O	0.33	0.36	0.40	0.32	0.41	0.38	0.35	0.35	0.36	0.34	0.37
K_2O	0.00	0.01	0.01	0.01	0.01	0.00	0.00	0.00	0.00	0.00	0.00
Cr_2O_3	1.34	1.20	1.13	1.30	1.29	1.32	1.17	1.34	1.22	1.14	1.32
NiO	0.05	0.02	0.00	0.04	0.03	0.00	0.02	0.01	0.01	0.03	0.01
Total	99.73	99.02	98.86	98.66	100.58	99.70	99.35	99.52	99.20	99.79	99.49
Mg*100/(Fe + Mg)	80.7	80.9	79.9	81.9	80.6	80.6	78.4	80.7	79.3	80.4	80.8
Si	1.903	1.904	1.900	1.900	1.919	1.919	1.919	1.907	1.911	1.917	1.906
Al(IV)	0.062	0.042	0.035	0.048	0.051	0.060	0.043	0.061	0.045	0.048	0.056
Al(VI)	0.097	0.096	0.100	0.100	0.081	0.081	0.081	0.093	0.089	0.083	0.094
Ti	0.014	0.012	0.015	0.014	0.015	0.013	0.014	0.015	0.015	0.015	0.014
Fe^{3+}	0.018	0.020	0.022	0.018	0.022	0.020	0.019	0.019	0.019	0.018	0.020
Fe^{2+}	0.108	0.107	0.114	0.104	0.102	0.106	0.127	0.106	0.124	0.112	0.103
Mn	0.003	0.005	0.004	0.003	0.004	0.003	0.004	0.003	0.004	0.004	0.004
Mg	0.939	0.958	0.962	0.989	0.926	0.933	0.948	0.937	0.978	0.959	0.927
Ca	0.848	0.860	0.853	0.823	0.866	0.849	0.839	0.847	0.809	0.834	0.868
Na	0.006	0.006	0.007	0.006	0.007	0.007	0.006	0.006	0.006	0.006	0.007
K	0.000	0.000	0.000	0.000	0.000	0.000	0.000	0.000	0.000	0.000	0.000
Cr	0.039	0.035	0.033	0.038	0.038	0.039	0.034	0.039	0.036	0.033	0.039
Ni	0.002	0.001	0.000	0.001	0.001	0.000	0.001	0.000	0.000	0.001	0.000
Mol.%											
Enstatite	49.48	49.67	49.77	51.54	48.78	49.33	49.43	49.48	51.07	50.22	48.74
Ferrosilite	5.67	5.54	5.89	5.42	5.38	5.59	6.62	5.60	6.45	5.88	5.41
Wollastonite	44.67	44.56	44.16	42.88	45.62	44.89	43.74	44.74	42.25	43.67	45.66

DISCUSSION

Sources and Geodynamics of Late Permian Mafic–Ultramafic Rocks

The zircon U–Pb ages of gabbro and olivine pyroxenite are 250.8 ± 0.8 Ma and 257.3 ± 0.7 Ma, respectively. These ages are consistent with field observations that mafic gabbro intersected the ultramafic olivine pyroxenite. In addition, the Paleo-Tethyan Anemaqen Ocean in EKOB are considered to begin northward subduction in the Late Permian before 260 Ma, and closed at the Middle Triassic (Mo et al., 2007; Li R. B. et al., 2012; Yang et al., 2013; Chen et al., 2017); and yet other scholars have proposed that the subduction of the Paleo-Tethys Ocean began at the Early Permian (Liu, 2014; Xiong et al., 2014; Chen et al., 2015), and closed in the Middle and Late Triassic as indicated by the deposit of a typical Upper Triassic Babaoshan molasse formation at that time (Wu et al., 2017). Therefore, the Xiwanggou complexes are believed to be formed in a subduction environment from Late Permian to Middle Triassic.

The trace element patterns of the Xiwanggou mafic-ultramafic intrusions are characterized by the depletion of HREE, Nb and Ta, and enrichment of Sr, Rb, Ba, and LREE (**Figure 9**), which

are clearly similar to those of island arc sulfide-bearing mafic intrusive rocks in the Tati and Selebi-Phikwe belts, eastern Botswana (Maier et al., 2008). In addition, the Late Permian-Early Triassic gabbroic and dioritic dykes from the EKOB display similar distribution patterns that are enriched in LILEs and depleted in HFSEs (Xiong et al., 2011a; Ding et al., 2014), which generally indicates a metasomatized mantle source in a subduction environment (Jiang et al., 2015; Kong et al., 2018). Therefore, the geochemical and geochronological data of the Xiwanggou complexes, together with the regional considerations, suggest that they record a northward subduction of the Paleo Tethys Ocean during Late Permian to Early Triassic (Mo et al., 2007; Xiong et al., 2011a; Zhang et al., 2012).

The AFC processes tend to obscure the potential distinctions of primary chemical signatures between the fertile and barren basalts. In this study, we calculated the AFC processes involved in the magma evolution controlled by the partition coefficient of minerals. In the conceptual model (**Figures 11A,B**), the geochemical evolution of the middle-late Permian rocks show different paths via two different mechanisms. This further indicates that some of the Late Permian mafic–ultrmafic magma first probably experienced dehydration partial melting controlled
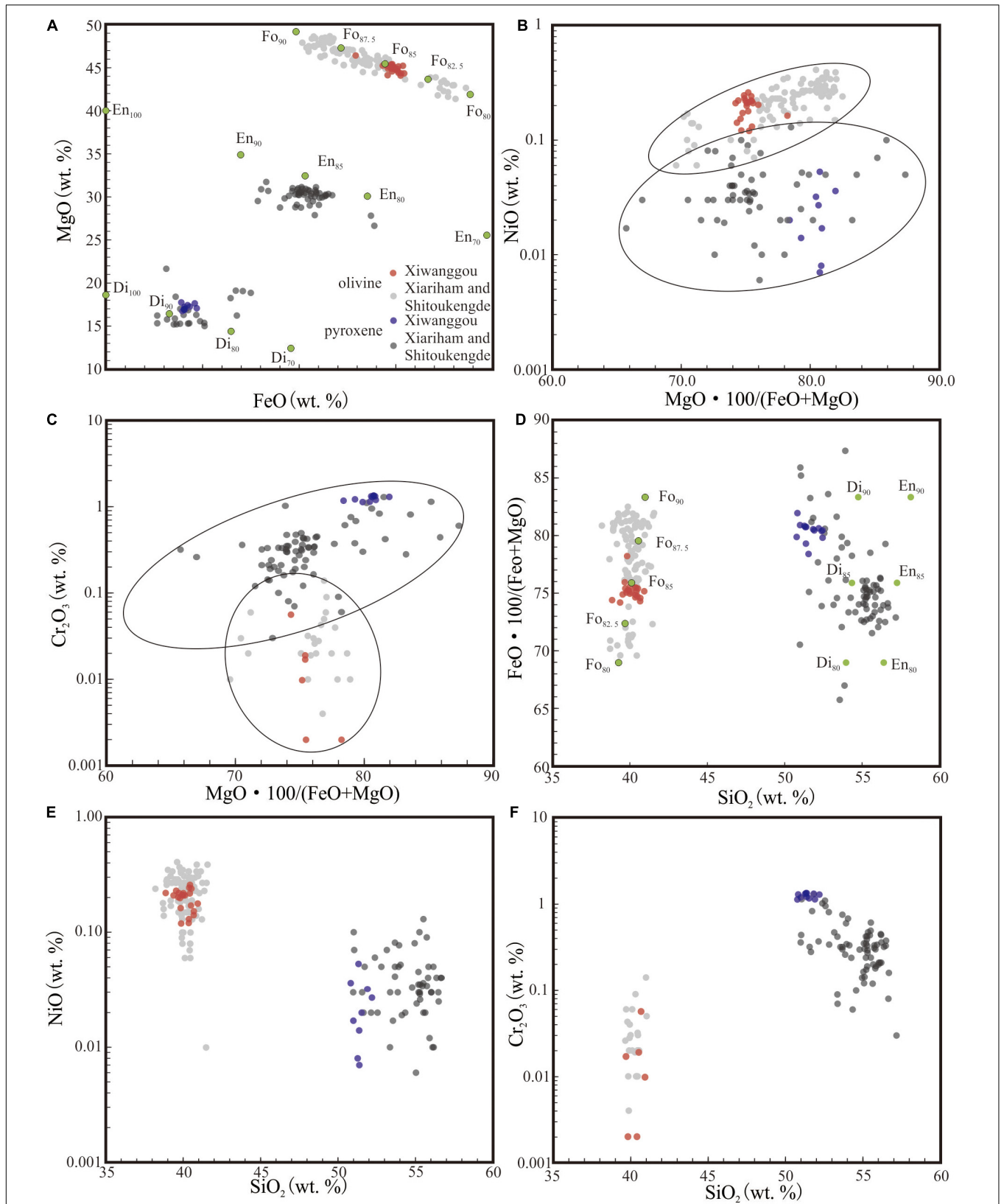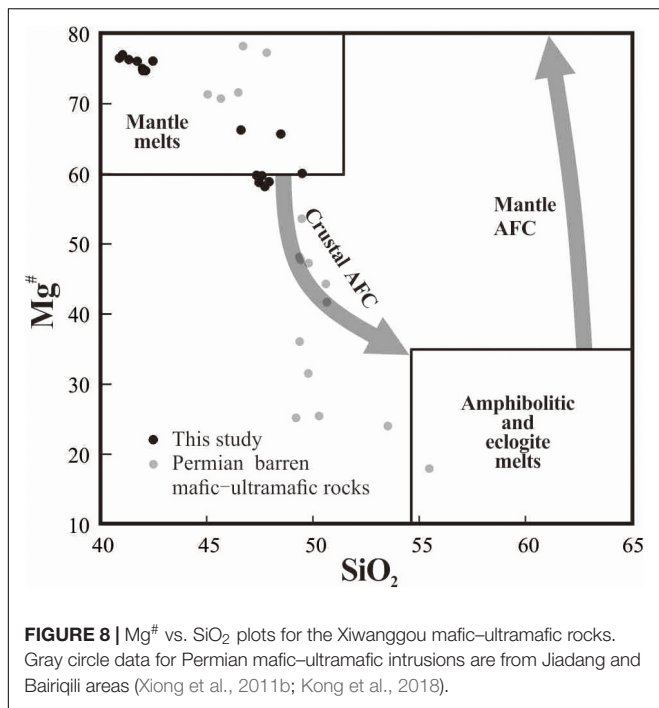
FIGURE 7 | Geochemical diagrams of olivine **(A,B)** and pyroxene **(C–F)** compositions. The blue circles are from the Xiwanggou mafic-ultramafic rocks, and the gray ones from the Xiarihamu and Shitoukengde basic–ultrabasic complexes.

FIGURE 8 | Mg# vs. SiO₂ plots for the Xiwanggou mafic–ultramafic rocks. Gray circle data for Permian mafic–ultramafic intrusions are from Jiadang and Bairiqili areas (Xiong et al., 2011b; Kong et al., 2018).

FIGURE 9 | Primitive mantle-normalized trace element patterns **(A)** and chondrite-normalized REE patterns **(B)**. Olivine gabbro normalizing values after Sun and McDonough (1989). The gray shadows show the spectrum of trace and REE elements from the Middle-Late Permian mafic–ultramafic intrusions developed in the East Kunlun Orogen (Xiong et al., 2011a; Kong et al., 2018).

by breakdown of amphibole in the mantle wedge, which usually occurs between ~825 and 1000°C at pressures between 0.5 and 2.0–2.5 GPa (Peacock et al., 1994). However, some other underwent an assimilation and fractional crystallization (AFC) process jointly controlled by 70% clinopyroxene (Cpx) and 30% garnet (Grt), and tended from lower crust to upper crust composition (**Figures 11A,B**).

The remarkable distinctions between contemporary fertile and barren rocks convey significant information on εNd(t) and (⁸⁷Sr/⁸⁶Sr)ᵢ values. The Xiwanggou ore-bearing intrusions with lower contents of SiO₂ and (⁸⁷Sr/⁸⁶Sr)ᵢ are believed to be less contaminated by crustal materials (**Figure 10A**; Arndt et al., 2005). However, the Bairiqili barren mafic-ultramafic intrusive rocks with relative high contents of SiO₂ and (⁸⁷Sr/⁸⁶Sr)ᵢ maybe indicate a mixing magma source between depleted subcontinental lithospheric mantle (SCLM) and lower crustal materials (**Figure 10A**; Xiong et al., 2011a; Liu et al., 2012). As the mafic microgranular enclaves (MMEs) captured by the Triassic granitoids in EKOB with similar SiO₂ contents and medium (⁸⁷Sr/⁸⁶Sr)ᵢ values are generally considered to be sourced from a mixing of subcontinental lithospheric mantle (SCLM) with EMII type mantle as well as felsic magma yielded by the partial melting of lower crust materials (Gao et al., 2015). Furthermore, the late Permian mafic-ultramafic rocks have similar trend paralleling to the EMII (enriched mantle II) features evolved from depleted mantle to lower crustal materials of basement, indicating a partial melting process of intensively depleted lithospheric mantle wedge above subducted slab as a consequence of injection of subduction-related fluid (**Figure 10B**). but the εNd(t) values of the Xiwanggou complex are close to zero and much more depleted than the contemporary barren mafic rocks in the
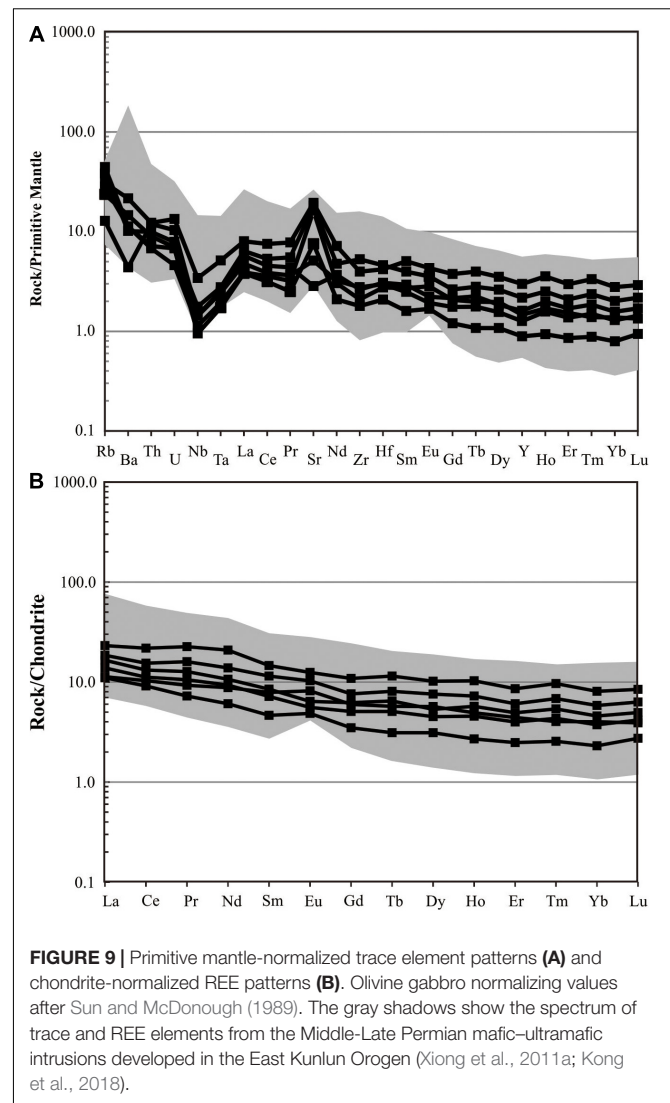
Bairiqili, which may be related to a relatively low assimilation–fractional crystallization (AFC) degree of lower crustal materials. This is consistent with the indication between varying Mg# and SiO₂ values (**Figure 8**). Nevertheless, the εNd(t) values of the contemporary barren mafic rocks show a similar spectrum to those of MMEs (**Figure 10B**), which further indicate that the magma are much more possible yielded by a partial melting process of metasomatized SCLM above subducted slab (Xiong et al., 2011a; Jiang et al., 2015; Peng et al., 2016; Li et al., 2018).

Many recent papers have proposed that the metasomatized portions of the SCLM are enriched in chalcophile and highly siderophile elements, and that partial melting of this part of the mantle are particularly capable of forming magmatic ore deposits (Fiorentini and Beresford, 2008; Richardson and Shirey, 2008; Zhang et al., 2008; Arndt, 2013). The contrasting geochemical signatures between fertile and barren may be attributed not only to the heterogeneity of SCLM sources, but also to the complexity of AFC processes during the interaction between SCLM and overlying crustal materials. The εHf(t) values of zircon crystals

from the Bairiqili and Yuejinshan non-mineralized mafic–ultramafic rocks are also consistent with crustal contamination of the parental magma to various degrees (**Figure 6**; Li et al., 2015, 2018). However, the εHf(t) values of the Xiwanggou are all positive between MORB and CHUR (**Figure 6**), which probably indicates a simple depleted mantle source with very slight mix. Apparently, the bulk-rock Nd and zircon Hf isotopes are decoupled in the Xiwanggou complex, in which the discrepancy between the extremely depleted Hf isotopes of zircons and the slight enriched Nd isotopes of bulk rocks demonstrate that zircons do not always capture the full history of magmatic system (Huang et al., 2019). In addition, the participation of amphibole and garnet in the melt producing processes maybe result in isotopic discrepancy between zircon and bulk-rocks (Huang et al., 2017, 2019).

The Xiwanggou fertile melts mainly experienced high degree partial melting of depleted SCLM controlled by amphibole dehydration, which can evolve with time to produce relatively low εNb(t) values at a high εHf(t) value. In addition, the slight right-dipping REE distribution patterns without obvious Eu anomalies and very low La/Yb ratios of bulk compositions indicates that the Xiwanggou basaltic magma probably experienced amphibole fractionation without garnet incorporation (Çoban, 2007; Dessimoz et al., 2012). Therefore, the favored interpretation may be that the Late Permian basalts was primarily yielded by the dehydration partial melting of amphibole above a subduction zone, and some melts would have directly arisen to a surficial depth along deep faults, e.g., Xiwanggou fertile complex; but some metasomatized melts would be detained at lower crust depth and further produced relatively siliceous magma due to fractional crystallization of Grt and Cpx, e.g., Bairiqili barren diabase-gabbros (**Figure 12**). The garnet-bearing residues after melt extraction were then transformed into juvenile lower crust materials, and evolved with time to produce high εHf(t) at a low εNd(t) value with elevation of Lu/Hf ratios (Huang et al., 2019).

The experimental petrologic evidence confirmed that the thermal and petrologic evolution of a mantle plume with time shows that the residues after liquidus extraction at the base of the lithosphere will contain garnet peridotite melt, as the following possible garnet-bearing residuum assemblages (Herzberg and O'Hara, 1998). Moreover, the pressure of garnet-bearing assemblages are reported at 1.9 to 2.8 GPa (Kinzler, 1997). Therefore, at pressures in the garnet peridotite stability field, pressure expands the stability field of garnet at the expense of all other crystalline phases, and the Al_2O_3 and HFSE content of magmas is reduced. There is evidence shows that the compositions of liquids produced by progressive equilibrium (batch) partial melting of a fertile mantle peridotite will have a wide range, and the first disappearance of aluminous garnet phase is usually the one leading to subsequent liquid evolution in [Lq + Ol + Opx + Cpx] by advanced melting, from 1 atm to about 3.0 GPa. Therefore, the middle-late Permian rocks record a complete geochemical trace from subduction to modification, indicating that the Middle-Late Permian rocks are much more likely influenced by the subduction environment. Such processes are most similar to that of the arc-related Ural-Alaska type

TABLE 5 | Whole rock Sr-Nd isotopic compositions of the Xiwanggou mafic–ultramafic complex.

Sample	t	Rb	Sr	$^{87}Rb/^{86}Sr$	$^{87}Sr/^{86}Sr$	2σ	$(^{87}Sr/^{86}Sr)i$	Sm	Nd	$^{147}Sm/^{144}Nd$	$^{143}Nd/^{144}Nd$	2σ	$(^{143}Nd/^{144}Nd)i$	ε Nd(0)	ε Nd(t)
XW-07-1	250	24.85	373.83	0.192377	0.706589	0.000007	0.705905	1.19	4.17	0.171750	0.512635	0.000015	0.512354	−0.06	0.74
XW-07-2	250	25.58	460.78	0.160606	0.707191	0.000009	0.706620	2.48	8.80	0.170502	0.512629	0.000009	0.512350	−0.18	0.66
XW-07-3	250	19.36	431.70	0.129798	0.706415	0.000008	0.705953	1.79	6.37	0.170205	0.512655	0.000011	0.512376	0.33	1.18
XW-09-1	257	42.03	178.95	0.679569	0.708157	0.000007	0.705672	0.79	3.02	0.158684	0.512524	0.000010	0.512257	−2.22	−0.98
XW-09-2	257	34.73	115.88	0.867154	0.708705	0.000006	0.705535	1.17	4.44	0.159790	0.512520	0.000014	0.512251	−2.30	−1.09
XW-09-3	257	11.35	68.96	0.476477	0.707875	0.000007	0.706133	1.38	5.40	0.154060	0.512544	0.000009	0.512285	−1.83	−0.43
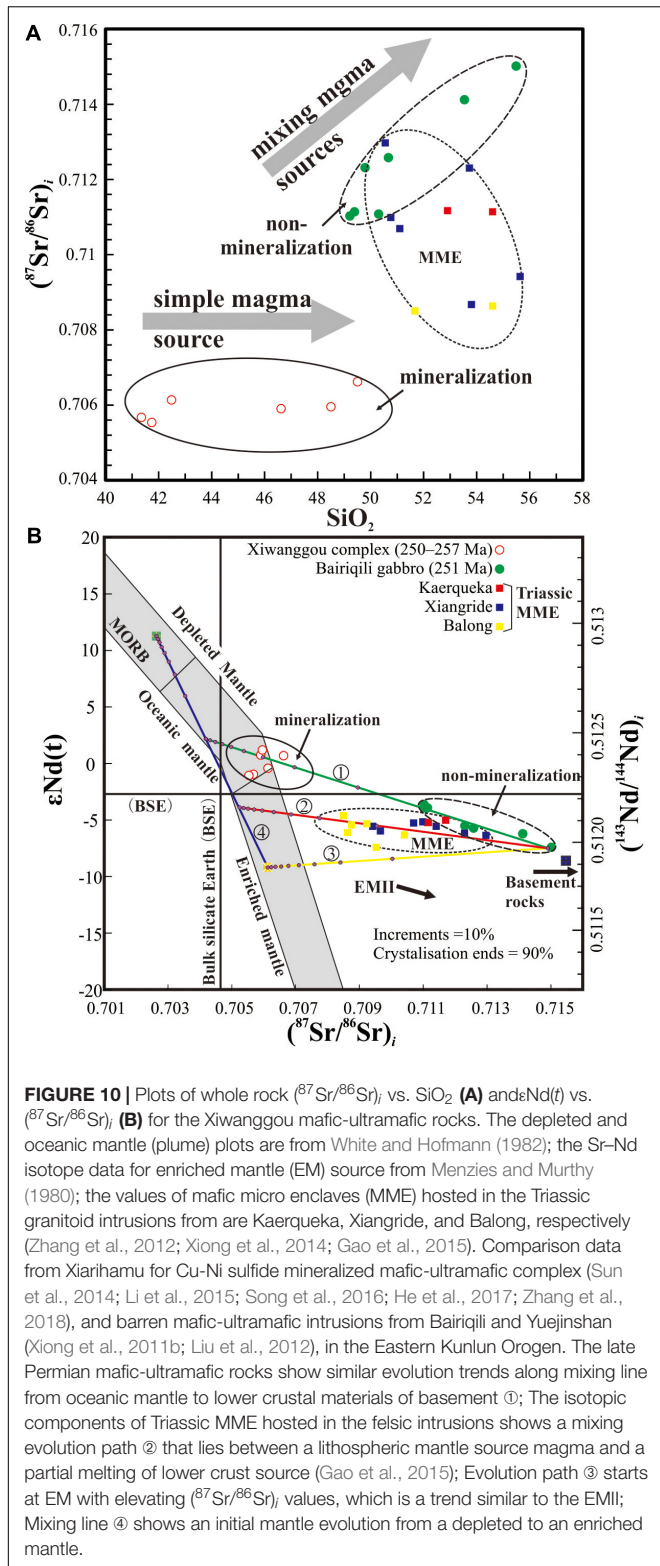
FIGURE 10 | Plots of whole rock $(^{87}Sr/^{86}Sr)_i$ vs. SiO_2 **(A)** and $\varepsilon Nd(t)$ vs. $(^{87}Sr/^{86}Sr)_i$ **(B)** for the Xiwanggou mafic-ultramafic rocks. The depleted and oceanic mantle (plume) plots are from White and Hofmann (1982); the Sr–Nd isotope data for enriched mantle (EM) source from Menzies and Murthy (1980); the values of mafic micro enclaves (MME) hosted in the Triassic granitoid intrusions from are Kaerqueka, Xiangride, and Balong, respectively (Zhang et al., 2012; Xiong et al., 2014; Gao et al., 2015). Comparison data from Xiarihamu for Cu-Ni sulfide mineralized mafic-ultramafic complex (Sun et al., 2014; Li et al., 2015; Song et al., 2016; He et al., 2017; Zhang et al., 2018), and barren mafic-ultramafic intrusions from Bairiqili and Yuejinshan (Xiong et al., 2011b; Liu et al., 2012), in the Eastern Kunlun Orogen. The late Permian mafic-ultramafic rocks show similar evolution trends along mixing line from oceanic mantle to lower crustal materials of basement ①; The isotopic components of Triassic MME hosted in the felsic intrusions shows a mixing evolution path ② that lies between a lithospheric mantle source magma and a partial melting of lower crust source (Gao et al., 2015); Evolution path ③ starts at EM with elevating $(^{87}Sr/^{86}Sr)_i$ values, which is a trend similar to the EMII; Mixing line ④ shows an initial mantle evolution from a depleted to an enriched mantle.
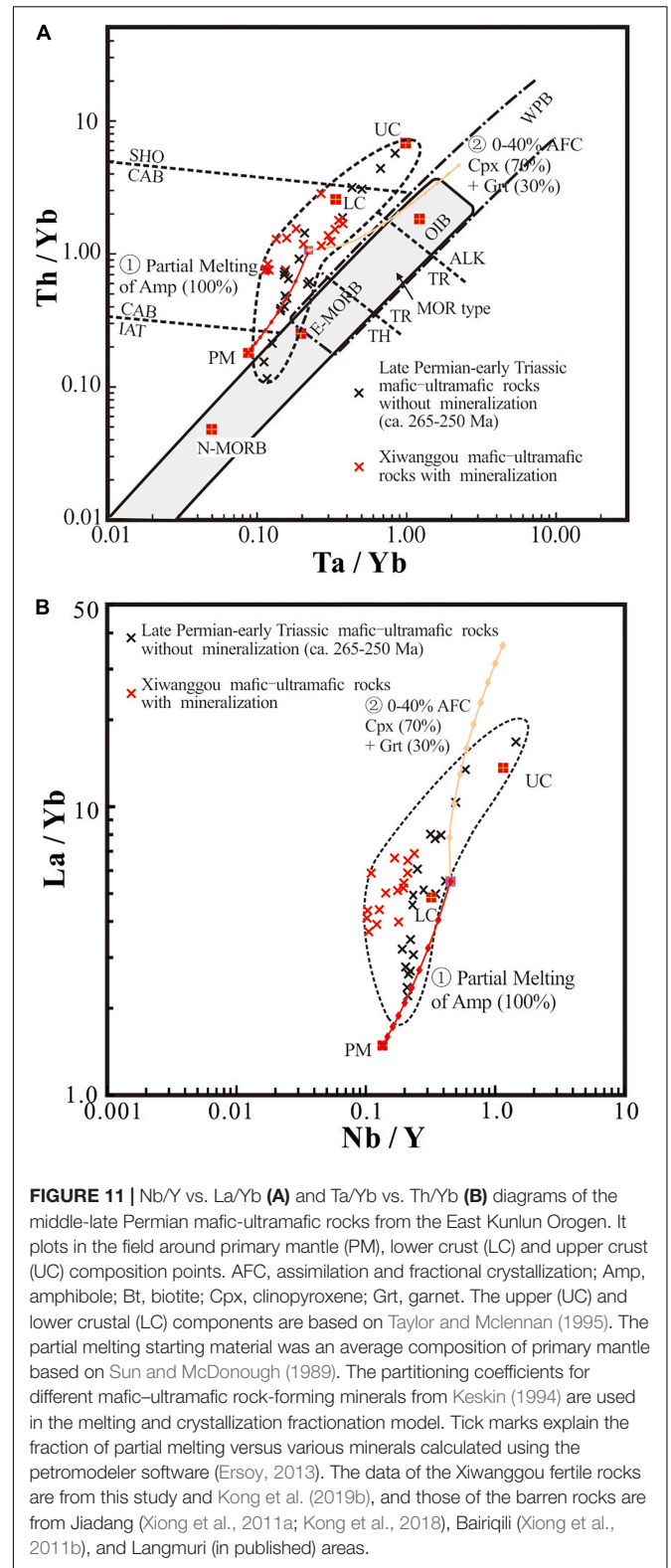
FIGURE 11 | Nb/Y vs. La/Yb **(A)** and Ta/Yb vs. Th/Yb **(B)** diagrams of the middle-late Permian mafic-ultramafic rocks from the East Kunlun Orogen. It plots in the field around primary mantle (PM), lower crust (LC) and upper crust (UC) composition points. AFC, assimilation and fractional crystallization; Amp, amphibole; Bt, biotite; Cpx, clinopyroxene; Grt, garnet. The upper (UC) and lower crustal (LC) components are based on Taylor and Mclennan (1995). The partial melting starting material was an average composition of primary mantle based on Sun and McDonough (1989). The partitioning coefficients for different mafic–ultramafic rock-forming minerals from Keskin (1994) are used in the melting and crystallization fractionation model. Tick marks explain the fraction of partial melting versus various minerals calculated using the petromodeler software (Ersoy, 2013). The data of the Xiwanggou fertile rocks are from this study and Kong et al. (2019b), and those of the barren rocks are from Jiadang (Xiong et al., 2011a; Kong et al., 2018), Bairiqili (Xiong et al., 2011b), and Langmuri (in published) areas.

complexes in Tianshan Orogen, which were produced by a high-degree of differentiation of the SCLM that was metasomatized by melts and/or fluids from the subduction (Su et al., 2012, 2014).

Olivine Fo value can be used as indicator of oxygen fugacity and temperature of hosted melt, which accounts to the activities of metallic Fe controlled by reducing conditions, and ferric

FIGURE 12 | Schematic diagram showing the tectonic evolutionary history of the Permian ultramafic–mafic complex and the corresponding mineralization of the East Kunlun Orogenic Belt. For explanation see text.
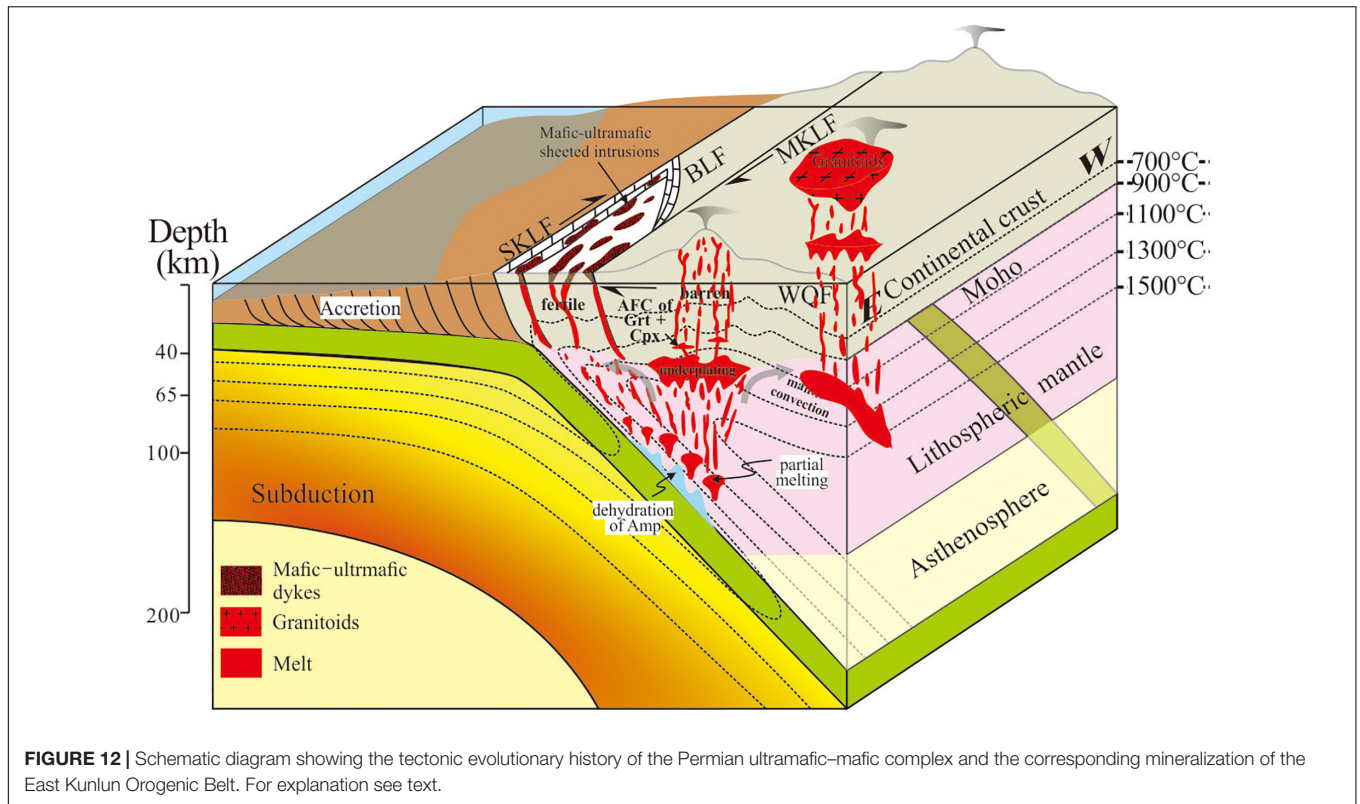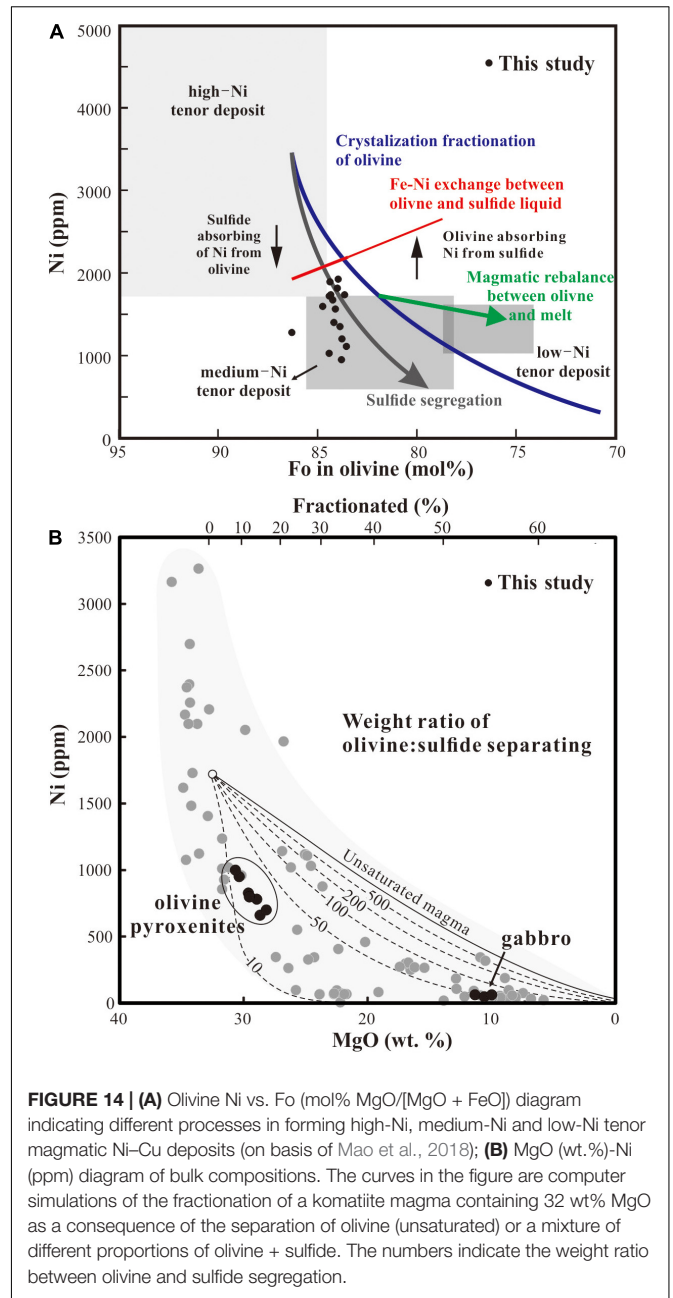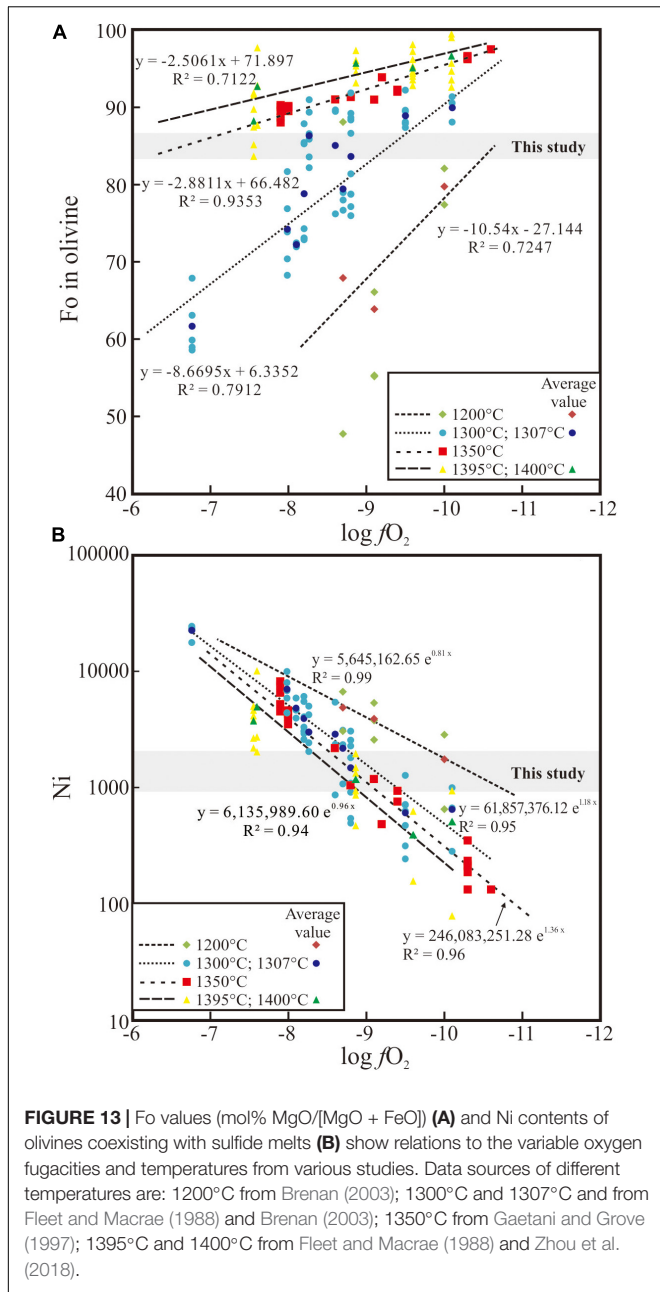
iron controlled by oxidizing conditions (Zhou et al., 2018). In addition, the exchange of Fe and Ni between olivine and sulfide melt is significantly controlled by the complex of temperature, sulfur fugacity, oxygen fugacity and nickel contents of sulfide melt (Brenan, 2003; Zhou et al., 2018), which is probably occurred in the deep continental lithosphere as mantle sulfide is likely molten in much of there (Zhou and Hirschmann, 2016). Although compositions of ascending mantle melt will be significantly affected by AFC processes, the Xiwanggou complex is justified to be slightly influenced in this study. Therefore, the olivine compositions from the Xiwanggou complex can be used to estimate the metling conditions of its mantle source. Compilation from previously published olivine-sulfide melt equilibration experiments (Fleet and Macrae, 1988; Gaetani and Grove, 1997; Brenan, 2003; Zhou et al., 2018), olivine Fo values and Ni contents show contrast relationships elevate with decreasing fO_2 at different temperatures (**Figures 13a,b**). On basis of the linear regressions, the moderate Fo values from this study suggests log fO_2 range of -10.57 ± 0.06 to -8.98 ± 0.07 between 1200 and 1300°C (**Figure 13a**), and the Ni contents give a similar logfO_2 range of -10.19 ± 0.28 to -9.02 ± 0.19 at a temperature range of 1200–1300°C (**Figure 13b**). Generally, the temperature of the hottest part of mantle wedge can reach ~1200–1350°C in continental magmatic arcs; and the crust-mantle boundary are typically at ~1 GPa and 1100°C (Grove et al., 2012). Moreover, the oxygen fugacity in Earth's mantle decrease with depth, within temperature range of 800–1400°C (Frost et al., 2004; Frost and Mccammon, 2008). Therefore, the parental magma of the

Xiwanggou complex derived from a dehydration partial melting of upper mantle wedge (ΔFMQ = -2 – 0 log units) rather than transition zone (ΔIW = 0) or deeper mantle (ΔIW = -1.4 log units and temperature above 1350°C), which was controlled by the breakdown of amphibole between the 1200 and 1300°C isotherms at relative shallow depths of 45–60 km (Peacock et al., 1994; Grove et al., 2012). The relatively reduced source may favor Ni relative to Fe in the melt owing to the great stability of the Ni_3S_2 species with greater metal/anion ratios [(Fe + Ni)/(S + O)] (Brenan and Caciagli, 2000; Kress, 2007).

Ore-Forming Potential of Xiwanggou Mafic–Ultramafic Magma

Several critical aspects for the genesis of the large and super-large magmatic sulfide ore deposits have been identified (Lambert et al., 1998; Naldrett, 1999; Mao et al., 2008; Song et al., 2011), and upgrading concentration and segregation of sulfide liquid from Ni-rich parent magma to an economic level is an imperative precondition (Li and Naldrett, 1999; Li et al., 2007; Mao et al., 2018). Generally, the mechanism of sulfide segregation affect subsolidus Fe–Ni exchange reaction between olivine and a sulfide liquid (Li et al., 2007; Mao et al., 2018). Olivines in contact with sulfide melt would react with sulfides, exchanging Ni and Fe (Li and Naldrett, 1999), which is an important mechanism for producing high Ni sulfide for picritic and basaltic magmas (relatively Ni-rich) (Brenan and Caciagli, 2000; Mao et al., 2018). The Fo values of the olivine from the Xiwanggou complex are covered by those of medium-Ni tenor deposit, and much lower than those from high tenor deposits, such as the Jinchuan and

FIGURE 13 | Fo values (mol% MgO/[MgO + FeO]) **(A)** and Ni contents of olivines coexisting with sulfide melts **(B)** show relations to the variable oxygen fugacities and temperatures from various studies. Data sources of different temperatures are: 1200°C from Brenan (2003); 1300°C and 1307°C and from Fleet and Macrae (1988) and Brenan (2003); 1350°C from Gaetani and Grove (1997); 1395°C and 1400°C from Fleet and Macrae (1988) and Zhou et al. (2018).

FIGURE 14 | (A) Olivine Ni vs. Fo (mol% MgO/[MgO + FeO]) diagram indicating different processes in forming high-Ni, medium-Ni and low-Ni tenor magmatic Ni–Cu deposits (on basis of Mao et al., 2018); **(B)** MgO (wt.%)-Ni (ppm) diagram of bulk compositions. The curves in the figure are computer simulations of the fractionation of a komatiite magma containing 32 wt% MgO as a consequence of the separation of olivine (unsaturated) or a mixture of different proportions of olivine + sulfide. The numbers indicate the weight ratio between olivine and sulfide segregation.

Xiariham deposits (**Figure 14A**; Zhang Z. W. et al., 2016; Zhou et al., 2016). In addition, the Xiwanggou complex shows a positive Fo-Ni correlation in olivines as a consequence of abundant Ni absorbed by olivine from sulfide and decreasing Fe contents in olivine affected by sulfide segregation (**Figure 14A**). Therefore, a strong sulfide segregation scale resulted in a medium tenor potential of the Xiwanggou deposit, whereas magmatic rebalance between olivine and melt will result in a low-Ni tenor deposit.

Ni and MgO contents in melt are significantly related to the ratios between olivine and sulfide segregation, and decrease with increasing fractionated degrees (**Figure 14B**). The Xiwanggou complex shows very low ratios of olivine and sulfide segregation that are mainly concentrated between 0.1 and 0.5 (**Figure 14B**).

The Ni and MgO contents of the Xiwanggou gabbro are obviously lower than the olivine pyroxenites, which accounts to the increasing melt fraction from olivine pyroxenites to gabbro (**Figure 14B**). Clinopyroxenes in the Xiwanggou olivine pyroxenites contain extremely high Cr_2O_3 contents and very low SiO_2 contents, which further indicates that the Xiwanggou complexes underwent relatively low degree fractionation in mantle, and would need more sulfur contents to achieve sulfur saturation (Liu et al., 2007).

The thermal structure of subduction zone was modeled to discuss the ore forming potential of the Xiwanggou mafic–ultramafic magma, as compare to those of the Ural–Alaska

type mafic–ultramafic intrusions in arc environments (Su et al., 2012; **Figure 12**). The subduction of oceanic slab continues from the Middle Permian to early Late Triassic in the EKOB (Yu et al., 2020), in which old and cool oceanic crust (<45 Ma) is subducted with a high angle, representing a rapid convergence (Peacock and Wang, 1999). Yao et al. (2018) suggested that the melting in cooler subduction zones is usually triggered and enhanced by the continuous addition of slab-derived fluids or melts, resulting in a relative low-Ni content in the melt, but warm subduction may produce melts with high Ni abundance. Therefore, we supposed that the Xiwanggou host rocks may reach medium potential for Cu–Ni sulfide mineralization, although its scientific significance are valuable.

Tectonic Control of Magmatic Conduit

Most economic magmatic Ni–Cu–(PGE) deposits have been interpreted to have formed indynamic lava channels or magma conduits (Zhou et al., 2004; Begg et al., 2010), which provide rapid and efficient magma transport to the crust without significant early sulfide segregation (Barnes and Lightfoot, 2005). Therefore, it is important to know the tectonic mechanism of the conduits for middle-late Permian mafic–ultramafic magmas in the EKOB as potential exploration targets.

In addition to the Xiwanggou complex, abundant similar types of the Late Permian- Middle Triassic mafic–ultramafic intrusions have been brought close to the surface as a result of more significant uplifting in the EKOB (Xiong et al., 2011a; Kong et al., 2018). All of these intrusions are located in the junction area between the EKOB and WQOB. Tectonic and geochronological constraints indicates that the subduction of the Paleo Tethys oceanic slab started during the Late Permian along the southern most Anemaqen fault (**Figure 1**), which resulted in large amounts of magmatism formed in the continental arc belt. Although the EKOB was in a suppressed setting as the subduction environment, significant local transpressional windows caused by the right-lateral strike-slip shearing action of the Wenquan (WQF) and South Kunlun faults (SKF) and a series of the secondary faults like the Longwakalu fault and bending Boluoer fault were formed in the South Kunlun forearc belt (**Figure 12**), which provided significant conduits for the large-scale magmatism and related magmatic metallogenesis (Begg et al., 2010). In addition, crustal deep faults have clearly played an important role in providing zones of weakness up which magma has ascended into crustal material. The characteristics of the tectonic setting are similar to those of the Early Permian Huangshan-Jing'erquan Ni–Cu belt in North Xinjiang (NW China), in which the right-lateral wrench tectonics characterized by crustal-scale shear zones most likely controlled and focused the intrusion of parent magmas (Branquet et al., 2012; Wu et al., 2018). It is therefore that the secondary tensional structures formed by large-scale regional shearing stress most likely provide a channel for the ascending of mantle-derived magma and also create a space for the formation of magma chambers in the crust. Furthermore, local transtensional-rifted spaces caused by large scale strike-slip shearing along

suture zones provide settings where deep, Moho-penetrating faults are available for reactivation, and accessing any dense mafic underplated material that might be residing at the base of the crust (Lightfoot and Evans-Lamswood, 2015; Barnes et al., 2016).

CONCLUSION

(1) The EKOB is characterized by two-stages of mafic–ultramafic magmatic activities associated with copper–nickel sulfide mineralization in the Late Silurian-Early Devonian and Middle-Late Permian;

(2) The late Permian Xiwanggou Ni–Cu-bearing mafic-ultramafic complexes are sheeted intrusions emplaced by injection of successive mafic-ultramafic magma batches.

(3) The parental magma of the Xiwanggou mafic–ultramafic complex derived from a source of SCLM in a cool subduction zone, which primarily experienced dehydration melting processes of amphiboles and subsequently underwent hydrated melting in the overlying mantle wedge and relatively reduced background.

(4) The Fe–Ni exchange between olivine and melt is significantly associated with the temperature and oxygen fugacity, which indicates that the magma were yielded in a temperature range of ca. 1200–1300°C and an oxygen fugacity range of ca. −10.57 to −8.98 (log unit).

(5) The transpressional windows as a consequence of Late Permian regional scale dextral strike-shearing activities, is considered as a conduit for the syn kinematic sheeted intrusion.

DATA AVAILABILITY STATEMENT

The original contributions presented in the study are included in the article/**Supplementary Material**, further inquiries can be directed to the corresponding author/s.

AUTHOR CONTRIBUTIONS

JZ and MY conceived of the presented idea. MY developed the theory and conducted the all experiments. HW and BL verified the analytical methods. CF, JL, HK, and ZZ helped the field geological survey work. All authors discussed the results and contributed to the final manuscript.

FUNDING

SUPPLEMENTARY MATERIAL

The Supplementary Material for this article can be found online at: https://www.frontiersin.org/articles/10.3389/feart.2021.666967/full#supplementary-material

REFERENCES

Arndt, N. (2013). The lithospheric mantle plays no active role in the formation of orthomagmatic ore deposits. *Econ. Geol.* 108, 1953–1970. doi: 10.2113/econgeo.108.8.1953

Arndt, N. T., Lesher, C. M., and Czamanske, G. K. (2005). Mantle-Derived Magmas and Magmatic Ni-Cu-(PGE) Deposits. *Econ. Geol.* 100, 5–24. doi: 10.5382/AV100.02

Barnes, S., and Lightfoot, P. C. (2005). Formation of magmatic nickel-sulfide ore deposits and processses affecting their copper and platinum-group element contents. *Econ. Geol.* 100, 179–213. doi: 10.5382/AV100.08

Barnes, S. J., Cruden, A. R., Arndt, N., and Saumur, B. M. (2016). The mineral system approach applied to magmatic Ni–Cu–PGE sulphide deposits. *Ore Geol. Rev.* 76, 296–316. doi: 10.1016/j.oregeorev.2015.06.012

Barnes, S. J., and Robertson, J. C. (2019). Time scales and length scales in magma flow pathways and the origin of magmatic Ni–Cu–PGE ore deposits. *Geosci. Front.* 10, 77–87. doi: 10.1016/j.gsf.2018.02.00

Begg, G. C., Hronsky, J. A., Arndt, N. T., Griffin, W. L., O'Reilly, S. Y., and Hayward, N. (2010). Lithospheric, cratonic, and geodynamic setting of Ni-Cu-PGE sulfide deposits. *Econ. Geol.* 105, 1057–1070.

Branquet, Y., Gumiaux, C., Sizaret, S., Barbanson, L., Wang, B., Cluzel, D., et al. (2012). Synkinematic mafic/ultramafic sheeted intrusions: emplacement mechanism and strain restoration of the Permian Huangshan Ni–Cu ore belt (Eastern Tianshan, NW China). *J. Asian Earth Sci.* 56, 240–257. doi: 10.2113/econgeo.105.6.1057

Brenan, J. M. (2003). Effects of fO_2, fS_2, temperature, and melt composition on Fe-Ni exchange between olivine and sulfide liquid: implications for natural olivine–sulfide assemblages. *Geochim. Cosmochim. Acta* 67, 2663–2681. doi: 10.1016/j.jseaes.2012.05.021

Brenan, J. M., and Caciagli, N. C. (2000). Fe–Ni exchange between olivine and sulphide liquid: implications for oxygen barometry in sulphide-saturated magmas. *Geochim. Cosmochim. Acta* 64, 307–320. doi: 10.1016/S0016-7037(02)01416-3

Cai, X. F., and Wei, Q. R. (2007). Stratigraphic sequence of oceanic islands and palinspastic reconstruction of the Wanbaogou Group in the eastern Kunlun orogenic belt. *J. Stratigr.* 31, 117–126. doi: 10.1016/S0016-7037(99)00278-1

Chen, G. C., Pei, X. Z., Li, R. B., Li, Z. C., Liu, C. N., Chen, Y. X., et al. (2017). Magma mixing and mingling for Xiangjiananshan granitic batholith at eastern area of the East Kunlun orogenic belt. *Acta Geol. Sin.* 91:63.

Chen, J. J., Fu, L. B., and Wei, J. H. (2016). Geochemical characteristics of late ordovician granodiorite in Gouli area, Eastern Kunlun orogenic belt, Qinghai province: implications on the evolution of Proto-Tethys ocean. *Earth Sci.* 41, 1863–1882. doi: 10.1111/1755-6724.13187

Chen, X. H., Gehrels, G., Yin, A., Zhou, Q., and Huang, P. H. (2015). Geochemical and Nd–Sr–Pb–O isotopic constrains on Permo–Triassic magmatism in eastern Qaidam Basin, northern Qinghai-Tibetan plateau: implications for the evolution of the Paleo-Tethys. *J. Asian Earth Sci.* 114, 674–692.

Çoban, H. (2007). Basalt magma genesis and fractionation in collision-and extension-related provinces: A comparison between eastern, central and western Anatolia. *Earth Sci. Rev.* 80, 219–238. doi: 10.1016/j.jseaes.2014.11.013

Dessimoz, M., Müntener, O., and Ulmer, P. (2012). A case for hornblende dominated fractionation of arc magmas: the Chelan complex (Washington Cascades). *Contrib. Min. Petrol.* 163, 567–589. doi: 10.1016/j.earscirev.2006.08.006

Ding, Q. F., Jiang, S. Y., and Sun, F. Y. (2014). Zircon U–Pb geochronology, geochemical and Sr–Nd–Hf isotopic compositions of the Triassic granite and diorite dikes from the Wulonggou mining area in the Eastern Kunlun Orogen, NW China: petrogenesis and tectonic implications. *Lithos* 205, 266–283. doi: 10.1007/s00410-011-0685-5

Dong, L. Q., Dong, G. C., Huang, H., and Bai, Y. (2016). Geochemical and zircon U-Pb dating characteristics and significance of the Tuluyin granites in the east of East Kunlun orogenic belt. *Geol. China* 43, 1737–1749. doi: 10.1016/j.lithos.2014.07.015

Dong, Y. P., He, D. F., Sun, S. S., Liu, X. M., Zhou, X. H., Zhang, F. F., et al. (2018). Subduction and accretionary tectonics of the East Kunlun orogen, western segment of the Central China Orogenic System. *Earth Sci. Rev.* 186, 231–261.

Ersoy, E. Y. (2013). PETROMODELER (Petrological Modeler): a Microsoft® Excel© spreadsheet program for modelling melting, mixing, crystallization and assimilation processes in magmatic systems. *Turk. J. Earth Sci.* 22, 115–125. doi: 10.1016/j.earscirev.2017.12.006

Fiorentini, M. L., and Beresford, S. W. (2008). Role of volatiles and metasomatized subcontinental lithospheric mantle in the genesis of magmatic Ni–Cu–PGE mineralization: insights from in situ H, Li, B analyses of hydromagmatic phases from the Valmaggia ultramafic pipe, Ivrea-Verbano Zone (NW Italy). *Terra Nova* 20, 333–340.

Fleet, M. E., and Macrae, N. D. (1988). Partition of Ni between olivine and sulfide: equilibria with sulfide-oxide liquids. *Contrib. Min. Petrol.* 100, 462–469. doi: 10.1111/j.1365-3121.2008.00825.x

Frost, D. J., Liebske, C., Langenhorst, F., Mccammon, C. A., Trønnes, R. G., and Rubie, D. C. (2004). Experimental evidence for the existence of iron-rich metal in the Earth's lower mantle. *Nature* 428:409. doi: 10.1007/BF00371375

Frost, D. J., and Mccammon, C. A. (2008). The redox state of Earth's mantle. *Annu. Rev. Earth Planet. Sci.* 36, 389–420. doi: 10.1038/nature02413

Gaetani, G. A., and Grove, T. L. (1997). Partitioning of moderately siderophile elements among olivine, silicate melt, and sulfide melt: constraints on core formation in the Earth and Mars. *Geochim. Cosmochim. Acta* 61, 1829–1846. doi: 10.1146/annurev.earth.36.031207.124322

Gan, C. H. (2014). *Petrology, Geochemistry, U-Pb Dating and Hf Isotopic Composition of Zircons in Igneous Rocks from East Kunlun Orogen, Qinghai.* Beijing: China University of Geosciences. doi: 10.1016/S0016-7037(97)00033-1

Gao, Y. B., Li, K., Qian, B., Li, W. Y., Li, D. S., Su, S. S., et al. (2015). The genesis of granodiorites and dark enclaves from the Kaerqueka deposit in east Kunlun belt: evidence from zircon U-Pb dating, geochemistry and Sr-Nd-Hf isotopic compositions. *Geol. China* 42, 646–662.

Grove, T. L., Till, C. B., and Krawczynski, M. J. (2012). The role of H2O in subduction zone magmatism. *Annu. Rev. Earth Planet. Sci.* 40, 413–439.

He, D. F., Dong, Y. P., Liu, X. M., Yang, Z., Sun, S. S., Cheng, B., et al. (2016). Tectono-thermal events in East Kunlun, Northern Tibetan Plateau: evidence from zircon U–Pb geochronology. *Gondwana Res.* 30, 179–190. doi: 10.1146/annurev-earth-042711-105310

He, S., Sun, F., Li, Y., Li, D., Yu, M., Qian, Y., et al. (2017). Geochemical and geochronological significance of the Binggounan garbbro in the Qiman Tage region, Qinghai province. *Bull. Mineral. Petrol. Geochem.* 36, 582–592. doi: 10.1016/j.jseaes.2016.07.019

Herzberg, C., and O'Hara, M. J. (1998). Phase equilibrium constraints on the origin of basalts, picrites, and komatiites. *Earth Sci. Rev.* 44, 39–79.

Hou, K. J., Li, Y. H., Zou, T. R., Qu, X. M., Shi, Y. R., and Xie, G. Q. (2007). Laser ablation-MC-ICP-MS technique for Hf isotope microanalysis of zircon and its geological applications. *Acta Petrol. Sin.* 23, 2595–2604.

Huang, H., Niu, Y., and Mo, X. (2017). Garnet effect on Nd-Hf isotope decoupling: Evidence from the Jinfosi batholith, Northern Tibetan Plateau. *Lithos* 274–275, 31–38. doi: 10.1016/S0012-8252(98)00021-X

Huang, H., Niu, Y., Teng, F. Z., and Wang, S. J. (2019). Discrepancy between bulk-rock and zircon Hf isotopes accompanying Nd-Hf isotope decoupling. *Geochim. Cosmochim. Acta* 259, 17–36. doi: 10.1016/j.lithos.2016.12.025

Jiang, C. F. (1992). Opening-closing evolution of the Kunlun Mountains. Opening closing tectonics of Kunlun Shan. *Geol. Memoirs Ser.* 5, 205–217. doi: 10.1016/j.gca.2019.05.031

Jiang, C. Y., Ling, J. L., Zhou, W., Du, W., Wang, Z. X., Fan, Y. Z., et al. (2015). Petrogenesis of the Xiarihamu Nibearing layered mafic-ultramafic intrusion, East Kunlun: implications for its extensional island arc environment. *Acta Petrol. Sin.* 31, 1117–1136.

Jiang, R. B., Chen, X. H., Dang, Y. Q., Yin, A., Wang, L. Q., Jiang, W. M., et al. (2008). Apatite fission track evidence for two phases Mesozoic-Cenozoic thrust faulting in eastern Qaidam Basin. *Chin. J. Geophys.* 51, 116–124.

Keskin, M. (1994). *Genesis of Collision-Related Volcanism on the Erzurum-kars Plateau, North Eastern Turkey.* Durham: Durham University.

Kinzler, R. J. (1997). Melting of mantle peridotite at pressures approaching the spinel to garnet transition: application to mid-ocean ridge basalt petrogenesis. *J. Geophys. Res. Solid Earth* 102, 853–874.

Kong, H. L., Li, J. C., Guo, X. Z., Yao, X. G., and Jia, Q. Z. (2019a). The discovery of Early Devonian pyroxene peridotite from the Xiwanggou magmatic Ni-Cu sulfide ore spot in East Kunlun Mountains. *Geol. China* 46, 205–206. doi: 10.1029/96JB00988

Kong, H. L., Li, Y. Z., Li, J. C., Jia, Q. Z., Guo, X. Z., and Zhang, B. (2019b). LA-ICP-MS zircon U-Pb dating and geochemical characteristics of the xiwanggou olivine pyroxenolite in East Kunlun. *J. Geomech.* 25, 440–452.

Kong, H. L., Li, J. C., Li, Y. Z., Jia, Q. Z., Guo, X. Z., and Zhang, B. (2018). Zircon U-Pb Dating and Geochemistry of the Jiadang Olivine Gabbro in the Eastern Section of East Kunlun,Qinghai Province and Their Geological Significance. *Acta Geol. Sin.* 92, 964–978.

Kong, H. L., Li, J. C., Li, Y. Z., Jia, Q. Z., and Yang, B. R. (2014). Geochemistry and zircon U-Pb geochronology of Annage diorite in the eastern section from East Kunlun in Qinghai province. *Geol. Sci. Technol. Inform.* 33, 11–17.

Kress, V. (2007). Thermochemistry of sulfide liquids III: Ni-bearing liquids at 1 bar. *Contrib. Min. Petrol.* 154, 191–204.

Lambert, D. D., Foster, J. G., Frick, L. R., Ripley, E. M., and Zientek, M. L. (1998). Geodynamics of magmatic Cu-Ni-PGE sulfide deposits; new insights from the Re-Os isotope system. *Econ. Geol.* 93, 121–136. doi: 10.1007/s00410-007-0187-7

Li, C. S., and Naldrett, A. J. (1999). Geology and petrology of the Voisey's Bay intrusion: reaction of olivine with sulfide and silicate liquids. *Lithos* 47, 1–31. doi: 10.2113/gsecongeo.93.2.121

Li, C. S., Naldrett, A. J., and Ripley, E. M. (2007). Controls on the Fo and Ni contents of olivine in sulfide-bearing Mafic/Ultramafic intrusions: principles, modeling, and examples from Voisey's Bay. *Earth Sci. Front.* 14, 177–183. doi: 10.1016/S0024-4937(99)00005-5

Li, C. S., Zhang, M. J., Fu, P., Qian, Z. Z., Hu, P. Q., and Ripley, E. M. (2012). The Kalatongke magmatic Ni–Cu deposits in the central Asian Orogenic Belt, NW China: product of slab window magmatism? *Min. Deposit.* 47, 51–67. doi: 10.1016/S1872-5791(07)60043-8

Li, C. S., Zhang, Z. W., Li, W. Y., Wang, Y. L., Sun, T., and Ripley, E. M. (2015). Geochronology, petrology and Hf–S isotope geochemistry of the newly-discovered Xiarihamu magmatic Ni–Cu sulfide deposit in the Qinghai–Tibet plateau, western China. *Lithos* 216, 224–240. doi: 10.1007/s00126-011-0354-7

Li, L., Sun, F. Y., Li, B. L., Li, S. J., Chen, G. J., Wang, W., et al. (2018). Geochronology, geochemistry and Sr-Nd-Pb-Hf isotopes of No. I complex from the Shitoukengde Ni-Cu sulfide deposit in the Eastern Kunlun Orogen, Western China: implications for the magmatic source, geodynamic setting and genesis. *Acta Geol. Sin.* 92, 106–126. doi: 10.1016/j.lithos.2015.01.003

Li, R. B., Pei, X. Z., Li, Z. C., Liu, Z. Q., Chen, G. C., Chen, Y. X., et al. (2012). Geological characteristics of Late Palaeozoic–Mesozoic unconformities and their response to some significant tectonic events in eastern part of Eastern Kunlun. *Earth Sci. Front.* 19, 244–254. doi: 10.1111/1755-6724.13497

Li, R. B., Pei, X. Z., Li, Z. C., Pei, L., Chen, G. C., Chen, Y. X., et al. (2017). Late cambrian SSZ-type ophiolites in acite zone, East Kunlun Orogen of Northern Tibet plateau: insights from Zircon U-Pb Isotopes and geochemistry of Oceanic Crust rocks. *Acta Geol. Sin.* 91, 66–67. doi: 10.1016/j.gsf.2011.05.005

Lightfoot, P. C., and Evans-Lamswood, D. (2015). Structural controls on the primary distribution of mafic–ultramafic intrusions containing Ni–Cu–Co–(PGE) sulfide mineralization in the roots of large igneous provinces. *Ore Geol. Rev.* 64, 354–386. doi: 10.1111/1755-6724.13189

Liu, B. (2014). *Petrogenesis and Geodynamic Setting of Permian to Triassic Mafic Rocks in the Yushu Area, Central Qinghai-Tibetan Plateau.* Wuhan: China University of Geoscience. doi: 10.1016/j.oregeorev.2014.07.010

Liu, B., Ma, C. Q., Zhang, J. Y., Xiong, F. H., Huang, J., and Jiang, H. A. (2012). Petrogenesis of Early Devonian intrusive rocks in the east part of Eastern Kunlun Orogen and implication for Early Palaeozoic orogenic processes. *Acta Petrol. Sin.* 28, 1785–1807.

Liu, J., Sun, F. Y., Li, L., Zhao, F. F., Wang, Y. D., Wang, S., et al. (2015). Geochronology, geochemistry and Hf isotopes of Gerizhuotuo complex intrusion in west of Anyemaqen suture zone. *Earth Sci. J. China Univ. Geosci.* 40, 965–981.

Liu, Y., Samaha, N., and Baker, D. R. (2007). Sulfur concentration at sulfide saturation (SCSS) in magmatic silicate melts. *Geochim. Cosmochim. Acta* 71, 1783–1799.

Liu, Y. J., Genser, J., Neubauer, F., Jin, W., Ge, X. H., Handler, R., et al. (2005). 40 Ar/39 Ar mineral ages from basement rocks in the Eastern Kunlun Mountains, NW China, and their tectonic implications. *Tectonophysics* 398, 199–224. doi: 10.1016/j.gca.2007.01.004

Long, X. P., Jin, W., Ge, W. C., and Yu, N. (2006). Zircon U-Pb geochronology and geological implications of the granitoids in Jinshuikou, East Kunlun, NW China. *Geochimica* 35, 333–345. doi: 10.1016/j.tecto.2005.02.007

Luo, Z. H., Deng, J. F., Cao, Y. Q., Guo, Z. F., and Mo, X. X. (1999). On late Paleozoic-early Mesozoic volcanism and regional tectonic evolution of Eastern Kunlun, Qinghai Province. *Geoscience* 13, 51–56.

Ma, C. Q., Xiong, F. H., Yin, S., Wang, L. X., and Gao, K. (2015). Intensity and cyclicity of orogenic magmatism: an example from a Paleo-Tethyan granitoid batholith, Eastern Kunlun, northern Qinghai-Tibetan Plateau. *Acta Petrol. Sin.* 31, 3555–3568.

Maier, W. D., Barnes, S., Chinyepi, G., Barton, J. M., Eglington, B., and Setshedi, I. (2008). The composition of magmatic Ni–Cu–(PGE) sulfide deposits in the Tati and Selebi-Phikwe belts of eastern Botswana. *Miner. Deposita* 43, 37–60.

Maier, W. D., and Groves, D. I. (2011). Temporal and spatial controls on the formation of magmatic PGE and Ni–Cu deposits. *Miner. Deposi.* 46, 841–857. doi: 10.1007/s00126-007-0143-5

Mao, J. W., Pirajno, F., Zhang, Z. H., Chai, F. M., Wu, H., Chen, S. P., et al. (2008). A review of the Cu–Ni sulphide deposits in the Chinese Tianshan and Altay orogens (Xinjiang Autonomous Region, NW China): principal characteristics and ore-forming processes. *J. Asian Earth Sci.* 32, 184–203. doi: 10.1007/s00126-011-0339-6

Mao, Y. J., Qin, K. Z., and Tang, D. M. (2018). Characteristics,genetic mechanism,and exploration perspective of Ni-rich sulfide in magmatic Ni-Cu systems. *Acta Petrol. Sin.* 34, 2410–2424. doi: 10.1016/j.jseaes.2007.10.006

Menzies, M., and Murthy, V. R. (1980). Enriched mantle: Nd and Sr isotopes in diopsides from kimberlite nodules. *Nature* 283:634.

Mo, X. X., Luo, Z. H., Deng, J., Yu, X., Liu, C., Yuan, W. M., et al. (2007). Granitoids and crustal growth in the East Kunlun orogenic belt. *Geol. J. China Univ.* 13, 403–414. doi: 10.1016/j.lithos.2006.10.005

Naldrett, A. J. (1999). World-class Ni-Cu-PGE deposits: key factors in their genesis. *Miner. Deposita* 34, 227–240.

Naldrett, A. J. (2013). *Magmatic Sulfide Deposits: Geology, Geochemistry and Exploration.* Berlin: Springer. doi: 10.1007/s001260050200

Peacock, S. M., Rushmer, T., and Thompson, A. B. (1994). Partial melting of subducting oceanic crust. *Earth Planet Sci. Lett.* 121, 227–244.

Peacock, S. M., and Wang, K. (1999). Seismic consequences of warm versus cool subduction metamorphism: Examples from southwest and northeast Japan. *Science* 286, 937–939. doi: 10.1016/0012-821X(94)90042-6

Peng, B., Sun, F., Li, B., Wang, G., Li, S., Zhao, T., et al. (2016). The geochemistry and geochronology of the Xiarihamu II mafic–ultramafic complex, Eastern Kunlun, Qinghai Province, China: implications for the genesis of magmatic Ni–Cu sulfide deposits. *Ore Geol. Rev.* 73, 13–28. doi: 10.1126/science.286.5441.937

Piña, R., Lunar, R., Ortega, L., Gervilla, F., Alapieti, T., and Martínez, C. (2006). Petrology and geochemistry of mafic-ultramafic fragments from the Aguablanca Ni-Cu ore breccia, southwest Spain. *Econ. Geol.* 101, 865–881. doi: 10.1016/j.oregeorev.2015.10.014

Qi, S. S. (2015). *Petrotectonic Assemblages and Tectonic Evolution of the East Kunlun Orogenic Belt in Qinghai Province.* Beijing: China University of Geosciences. doi: 10.2113/gsecongeo.101.4.865

Ren, E. F., Zhang, G. L., Qiu, W., Li, H. X., and Sun, Z. H. (2012). Characteristics of geochemistry and tectonic significance of Caledonian granite in the Maerzheng region in the south area of East Kunlun. *Geoscience* 26, 36–44.

Ren, H. D., Wang, T., Zhang, L., Wang, X. X., Huang, H., Feng, C. Y., et al. (2016). Ages, sources and tectonic settings of the Triassic igneous rocks in the easternmost segment of the East Kunlun orogen, central China. *Acta Geol. Sin.* 90, 641–668.

Richardson, S. H., and Shirey, S. B. (2008). Continental mantle signature of Bushveld magmas and coeval diamonds. *Nature* 453, 910–913. doi: 10.1111/1755-6724.12696

Rubatto, D., and Gebauer, D. (2000). "Use of cathodoluminescence for U-Pb zircon dating by ion microprobe: some examples from the Western Alps," in *Cathodoluminescence in Geosciences*, eds M. Pagel, V. Barbin, P. Blanc, and D. Ohnenstetter (Heidelberg: Springer), 373–400. doi: 10.1038/nature07073

Sappin, A., Constantin, M., and Clark, T. (2011). Origin of magmatic sulfides in a Proterozoic island arc—an example from the Portneuf–Mauricie Domain, Grenville Province, Canada. *Miner. Deposita* 46, 211–237. doi: 10.1007/978-3-662-04086-7_15

Shao, F. L., Niu, Y. L., Liu, Y., Chen, S., Kong, J. J., and Duan, M. (2017). Petrogenesis of Triassic granitoids in the East Kunlun Orogenic Belt, northern Tibetan Plateau and their tectonic implications. *Lithos* 282, 33–44. doi: 10.1007/s00126-010-0321-8

Shi, B., Zhu, Y. H., Zhong, Z. Q., and Jian, K. K. (2016). Petrological, geochemical characteristics and geological significance of the Caledonian peraluminous granites in Heihai region, Eastern Kunlun. *Earth Sci.* 41, 35–54. doi: 10.1016/j.lithos.2017.03.002

Sláma, J., Košler, J., Condon, D. J., Crowley, J. L., Gerdes, A., Hanchar, J. M., et al. (2008). Plešovice zircon — a new natural reference material for U–Pb and Hf isotopic microanalysis. *Chem. Geol.* 249, 1–35.

Song, X., and Li, X. (2009). Geochemistry of the Kalatongke Ni–Cu–(PGE) sulfide deposit, NW China: implications for the formation of magmatic sulfide mineralization in a postcollisional environment. *Miner. Deposita* 44, 303–327. doi: 10.1016/j.chemgeo.2007.11.005

Song, X. Y., Wang, Y. S., and Chen, L. M. (2011). Magmatic Ni-Cu-(PGE) deposits in magma plumbing systems: features, formation and exploration. *Geosci. Front.* 2, 375–384. doi: 10.1007/s00126-008-0219-x

Song, X. Y., Xiao, J. F., Dan, Z., Zhu, W. G., and Chen, L. M. (2010). New insights on the formation of magmatic sulfide deposits in magma conduit system. *Earth Sci. Front.* 17, 153–163. doi: 10.1016/j.gsf.2011.05.005

Song, X. Y., Yi, J. N., Chen, L. M., She, Y. W., Liu, C. Z., Dang, X. Y., et al. (2016). The Giant Xiarihamu Ni-Co sulfide deposit in the East Kunlun Orogenic Belt, Northern Tibet Plateau, China. *Econ. Geol.* 111, 29–55. doi: 10.1007/978-3-662-08444-1

Su, B., Qin, K., Zhou, M., Sakyi, P. A., Thakurta, J., Tang, D., et al. (2014). Petrological, geochemical and geochronological constraints on the origin of the Xiadong Ural–Alaskan type complex in NW China and tectonic implication for the evolution of southern Central Asian Orogenic Belt. *Lithos* 200, 226–240. doi: 10.2113/econgeo.111.1.29

Su, B. X., Qin, K. Z., Sakyi, P. A., Malaviarachchi, S. P., Liu, P. P., Tang, D. M., et al. (2012). Occurrence of an Alaskan-type complex in the Middle Tianshan Massif, Central Asian Orogenic Belt: inferences from petrological and mineralogical studies. *Int. Geol. Rev.* 54, 249–269. doi: 10.1016/j.lithos.2014.05.005

Sun, F. Y., Li, B. L., Li, S. J., Zhao, D. W., Ao, Z., and Yang, Q. A. (2014). Petrography, zircon U-Pb geochronology and geochemistry of the mafic-ultramafic intrusion in Xiarihamu Cu-Ni deposit from East Kunlun, with implications for geodynamic setting. *Earth Sci. Front.* 21, 381–401. doi: 10.1080/00206814.2010.543009

Sun, S. S., and McDonough, W. F. (1989). Chemical and isotopic systematics of oceanic basalts: implications for mantle composition and processes. *Geol. Soc. Lond. Spec. Public.* 42, 313–345. doi: 10.1111/1755-6724.12371_22

Taylor, S. R., and Mclennan, S. M. (1995). The geochemical evolution of the continental crust. *Rev. Geophys.* 33, 241–265. doi: 10.1144/GSL.SP.1989.042.01.19

Wang, C. Y., Zhang, Z. W., Zhang, C. J., Chen, C. H., and Qian, B. (2020). Constraints on sulfide saturation by crustal contamination in the Shitoukengde Cu-Ni deposit, East Kunlun orogenic belt, northern Qinghai-Tibet Plateau, China. *Geosci. J.* 1–15. doi: 10.1029/95RG00262

Wang, G., Sun, F., Bile, L. I., Shijin, L. I., Zhao, J., Cong, A. O., et al. (2014). Petrography, Zircon U-Pb geochronology and geochemistry of the mafic-ultramafic intrusion in Xiarihamu Cu-Ni deposit from East Kunlun, with

implications for geodynamic setting. *Acta Geol. Sin.* 88, 318–319. doi: 10.1007/s12303-020-0025-8

Wang, G., Sun, F. Y., Li, B. L., Li, S. J., Zhao, J. W., Qian, Y., et al. (2013). Zircon U-Pb Geochronology and geochemistry of the early devonian syenogranite in the Xiarihamu Ore district from East Kunlun, with Implications for the geodynamic setting. *Geotecton. Metallogen.* 37, 685–697. doi: 10.1111/1755-6724.12371_22

Wang, T., Li, B., Chen, J., Wang, J. S., Li, W. F., and Jin, T. T. (2016). Characteristics of chronology and geochemistry of the early Silurian monzogranite in the Wulonggou area, East Kunlun and its geological significance. *J. Mineral. Petrol.* 36, 62–70.

White, W. M., and Hofmann, A. W. (1982). Sr and Nd isotope geochemistry of oceanic basalts and mantle evolution. *Nature* 296:821. doi: 10.1007/s00410-016-1272-6

Wiedenbeck, M., Alle, P., Corfu, F., Griffin, W. L., Meier, M., Oberli, F. V., et al. (1995). Three natural zircon standards for U-Th-Pb, Lu-Hf, trace element and REE analyses. *Geostand. Newslett.* 19, 1–23. doi: 10.1038/296821a0

Wu, C. Z., Xie, S. W., Gu, L. X., Samson, I. M., Yang, T., Lei, R. X., et al. (2018). Shear zone-controlled post-magmatic ore formation in the Huangshandong Ni–Cu sulfide deposit, NW China. *Ore Geol. Rev.* 100, 545–560. doi: 10.1111/j.1751-908X.1995.tb00147.x

Wu, J., Lan, C. L., and Li, J. L. (2005). Geochemical characteristics and tectonic setting of volcanic rocks in the Muztag ophiolitic mélange, East Kunlun Mountains, Xinjiang, China. *Geol. Bull. China* 24, 1157–1161. doi: 10.1016/j.oregeorev.2017.02.015

Wu, R. C., Gu, X. X., Zhang, Y. M., He, G., Kang, J. Z., Yu, F. C., et al. (2017). The sedimentary geochemical records about the tectonic evolution of the East Kunlun Orogenic Belt from early Paleozoic to early Mesozoic. *Geoscience* 31, 716–733.

Wu, S. F., Chen, L. B., Ren, W. K., Zhang, H. Q., Wang, S. H., and Ding, C. W. (2012). Discovery of rapakivite granite and its geological implication in Qimantage. *J. Qinghai Univ.* 30, 49–54.

Xiong, F. H., Ma, C. Q., Zhang, J. Y., and Liu, B. (2011a). LA-ICP-MS zircon U-Pb dating, elements and Sr-Nd-Hf isotope geochemistry of the Early Mesozoic mafic dyke swarms in East Kunlun orogenic belt. *Acta Petrol. Sin.* 27, 3350–3364.

Xiong, F. H., Ma, C. Q., Zhang, J. Y., Liu, B., Jiang, H. A., and Huang, J. (2011b). Zircon LA-ICP-MS U-Pb dating of Bairiqili gabbro pluton in East Kunlun orogenic belt and its geological significance. *Geol. Bull. China* 30, 1196–1202.

Xiong, F. H., Ma, C. Q., Zhang, J. Y., Liu, B., and Jiang, H. A. (2014). Reworking of old continental lithosphere: an important crustal evolution mechanism in orogenic belts, as evidenced by Triassic I-type granitoids in the East Kunlun orogen, Northern Tibetan Plateau. *J. Geol. Soc. Lond.* 171, 847–863.

Xu, X., Song, S. G., and Su, L. (2016). Formation age and tectonic significance of the Wanbaogou basalts in the middle East Kunlun orogenic belt. *Acta Petrol. Mineral.* 35, 965–980. doi: 10.1144/jgs2013-038

Yang, J. S., Jiang, C. F., Feng, B. G., Zhu, Z. Z., Zhao, M., Shi, X. D., et al. (1986). An outline on the tectonics of the Kunlun region. *Bull. Instit. Geol. Chin. Acad. Geol. Sci.* 2:10.

Yang, Y., Li, B. L., Xu, Q. L., and Zhang, B. S. (2013). Zircon U-Pb ages and its geological significance of the monzonitic granite in the Aikengdelesite, Eastern Kunlun. *Northwestern Geol.* 1, 56–62.

Yao, Z. S., Qin, K. Z., and Mungall, J. E. (2018). Tectonic controls on Ni and Cu contents of primary mantle-derived magmas for the formation of magmatic sulfide deposits. *Am. Miner.* 103, 1545–1567.

Ye, Z. F., Wang, J., Wang, B. Z., Suo, Y. X., Song, T. Z., and Ma, Y. S. (2004). Discovery and primarily research of the Early-Middle Devonian strata in mount Bukedaban district in west-middle section of East Kunlun Mts. *Northwestern Geol.* 37, 13–18. doi: 10.2138/am-2018-6392

Yu, M., Dick, M. J., Feng, C., Li, B., and Wang, H. (2020). The tectonic evolution of the East Kunlun Orogen, northern Tibetan Plateau: a critical review with an integrated geodynamic model. *J. Asian Earth Sci.* 191:104168.

Zhang, A. K., Liu, Y. L., Liu, G. L., Wei, Y. X., Liu, Z. G., Dai, W., et al. (2015). Mineralization types and prospecting potential of Binggounan area in Qimantage metallogenic belt, Qinghai procince. *Northwestern Geol.* 48, 125–140. doi: 10.1016/j.jseaes.2019.104168

Zhang, D. X., Wei, X. L., Zeng, X. P., Wang, W., Yu, X. L., Wang, T., et al. (2016). Geochemical characteristics and tectonic setting analysis of middle devonian intermediate-acid intrusive rock in the Gashundawu area, eastern Kunlun belt. *Miner. Explorat.* 7, 612–623.

Zhang, H. F., Zhang, L., Harris, N., Jin, L. L., and Yuan, H. L. (2006). U–Pb zircon ages, geochemical and isotopic compositions of granitoids in Songpan-Garze fold belt, eastern Tibetan Plateau: constraints on petrogenesis and tectonic evolution of the basement. *Contrib. Miner. Petrol.* 152, 75–88.

Zhang, J. Y., Ma, C. Q., Xiong, F. H., and Liu, B. (2012). Petrogenesis and tectonic significance of the Late Permian–Middle Triassic calc-alkaline granites in the Balong region, eastern Kunlun Orogen, China. *Geol. Mag.* 149, 892–908. doi: 10.1007/s00410-006-0095-2

Zhang, M., Reilly, S. Y. O., Wang, K. L., Hronsky, J., and Griffin, W. L. (2008). Flood basalts and metallogeny: The lithospheric mantle connection. *Earth Sci. Rev.* 86, 145–174. doi: 10.1017/S0016756811001142

Zhang, M. J., Liu, Y. G., Chen, A. P., Liang, K. K., Yang, Y., and Xu, W. (2021). The tectonic links between Palaeozoic eclogites and mafic magmatic Cu-Ni-Co mineralization in East Kunlun orogenic belt, western China. *Int. Geol. Rev.* 6, 1–21. doi: 10.1016/j.earscirev.2007.08.007

Zhang, Y. F., Pei, X. Z., Ding, S. P., Li, R. B., Feng, J. Y., Sun, Y., et al. (2010). LA-ICP-MS zircon U-Pb age of quartz diorite at the Kekesha area of Dulan County, eastern section of the East Kunlun orogenic belt, China and its significance. *Geol. Bull. China* 29, 79–85. doi: 10.1080/00206814.2021.1885504

Zhang, Z., Wang, Y., Qian, B., Liu, Y., Zhang, D., Lü, P., et al. (2018). Metallogeny and tectonomagmatic setting of Ni-Cu magmatic sulfide mineralization, number I Shitoukengde mafic-ultramafic complex, East Kunlun Orogenic Belt, NW China. *Ore Geol. Rev.* 96, 236–246.

Zhang, Z. W., Tang, Q. Y., Li, C. S., Wang, Y. L., and Ripley, E. M. (2016). Sr-Nd-Os-S isotope and PGE geochemistry of the Xiarihamu magmatic sulfide deposit in the Qinghai-Tibet plateau, China. *Miner. Deposita* 52, 51–68. doi: 10.1016/j.oregeorev.2018.04.027

Zhao, F. F., Sun, F. Y., and Liu, J. L. (2017). Zircon U-Pb geochronology and geochemistry of the gneissic granodiorite in Manite area from East Kunlun,

with implications for geodynamic setting. *Earth Sci.* 42, 927–1044. doi: 10.1007/s00126-016-0645-0

Zhao, Z. M., Ma, H. D., Wang, B. Z., Bai, Y. S., Li, R. S., and Ji, W. H. (2008). The evidence of intrusive rocks about collision-orogeny during Early Devonian in Eastern Kunlun area. *Geol. Rev.* 54, 1–11.

Zhou, M. F., Lesher, C. M., Yang, Z., Li, J., and Sun, M. (2004). Geochemistry and petrogenesis of 270 Ma Ni–Cu–(PGE) sulfide-bearing mafic intrusions in the Huangshan district, Eastern Xinjiang, Northwest China: implications for the tectonic evolution of the Central Asian orogenic belt. *Chem. Geol.* 209, 233–257.

Zhou, W., Wang, B. Y., Xia, M. Z., Xia, Z. D., Jiang, C. Y., Dong, J., et al. (2016). Mineralogical characteristics of Shitoukengde mafic-ultramafic intrusion and analysis of its metallogenic potential, East Kunlun. *Acta Petrol. Mineral.* 35, 81–96. doi: 10.1016/j.chemgeo.2004.05.005

Zhou, Z., Handt, A. V. D., and Hirschmann, M. M. (2018). An experimental study of Fe–Ni exchange between sulfide melt and olivine at upper mantle conditions: implications for mantle sulfide compositions and phase equilibria. *Contrib. Mineral. Petrol.* 173:19.

Zhou, Z., and Hirschmann, M. M. (2016). Experimental constraints on mantle sulfide melting up to 8 GPa. *Am. Miner.* 101, 181–192. doi: 10.1007/s00410-018-1444-7